

# Preliminary Measurements on the BOLT Geometry in the Supersonic Low Disturbance Tunnel

Andrew N. Leidy\*, Amanda Chou†  
NASA Langley Research Center, Hampton, VA 23681

Jonathan Davami‡, Thomas J. Juliano§  
University of Notre Dame, Notre Dame, IN, 46556

Experiments were performed in the Mach 3.5 Supersonic Low Disturbance Tunnel on the BOundary-Layer Transition (BOLT) geometry. The goal of this campaign was to assess changes to the transition front by varying the freestream noise and the model surface quality. The model was printed of polycarbonate and is 30% scale of the flight geometry. It was tested under noisy and quiet conditions at different streamwise positions in the tunnel and was also tested before and after improvements were made to the model surface through sanding and gap reduction. Pitch and yaw angles were nominally zero. The model surface temperature was measured using infrared thermography and thermocouples as the unit Reynolds number was swept from  $4.75 - 15.8 \times 10^6 \text{ m}^{-1}$ . Boundary-layer transition was observed near the midspan of the model for unit Reynolds numbers above  $10 \times 10^6 \text{ m}^{-1}$  in quiet flow, while transition was already observed on the shoulders below  $5 \times 10^6 \text{ m}^{-1}$  in noisy flow. The model surface enhancements improved the symmetry of the transition front for quiet flow but made only slight differences for noisy flow. In quiet flow, the impact of streamwise positioning on transition was more significant on the model shoulders compared to the central region. The difference in the shoulder heating was likely due to variation in noise radiated from the nozzle sidewalls. The total temperature and initial wall temperatures were near 300 K and 293 K, respectively, which generally resulted in negative convective heat-flux values into the model. Hot-wire anemometry was also utilized to characterize the freestream and to conduct a planar survey near the base of the model for the  $7.92 \times 10^6 \text{ m}^{-1}$  quiet condition. The survey captured the thickening of the boundary layer at the centerline and the vortical nature of the flow outboard of it. Spectral analysis of the mass-flux fluctuations near the midspan demonstrates that the boundary layer is laminar and suggests that the thick boundary layer caused the relatively warm centerline observed in the infrared images.

## Nomenclature

$c_p$	specific heat at constant pressure, $\text{J}\cdot\text{kg}^{-1}\cdot\text{K}^{-1}$
$f$	frequency, $\text{s}^{-1}$
$G_{xx}$	normalized power spectral density, s
$k$	thermal conductivity, $\text{W}\cdot\text{m}^{-1}\cdot\text{K}^{-1}$
$L$	model length, 260 mm
$M$	Mach number
$Q$	heat flux, $\text{W}\cdot\text{m}^{-2}$
$R_q$	rms roughness height, $\mu\text{m}$
$Re$	unit Reynolds number, $\text{m}^{-1}$
$t$	time, s
$T$	temperature, K
$u$	streamwise velocity component, $\text{m}\cdot\text{s}^{-1}$
$x$	body-fixed streamwise coordinate from nosetip, mm

\*Research Aerospace Engineer, Flow Physics and Control Branch, M.S. 170, Member AIAA.

†Research Aerospace Engineer, Flow Physics and Control Branch, M.S. 170, Associate Fellow AIAA.

‡Graduate Student, Aerospace and Mechanical Engineering Department, Student Member AIAA.

§Associate Professor, Department of Aerospace and Mechanical Engineering, Associate Fellow AIAA.

$X$	nozzle-fixed streamwise coordinate from throat, mm
$y$	local vertical coordinate, mm
$Y$	nozzle-fixed vertical coordinate from centerline, mm
$z$	body-fixed spanwise coordinate, mm
$Z$	nozzle-fixed lateral coordinate from centerline, mm
$\alpha$	thermal diffusivity, $\text{mm}^2 \cdot \text{s}^{-1}$
$\epsilon$	emissivity
$\rho$	density, $\text{kg} \cdot \text{m}^{-3}$
$\sigma$	standard deviation
$(\xi, \eta, \zeta)$	relative streamwise, wall normal, and spanwise distances, mm or $\mu\text{m}$

## I. Introduction

HEAT transfer is a primary concern for high-speed vehicles and can be nearly an order of magnitude higher for transitional or turbulent boundary layers compared to their laminar counterparts. The thermal protection system, and its associated weight, may be reduced in regions of extended laminar flow if there is confidence in heating predictions. Weight reduction improves fuel efficiency and allows for the payload to be increased for more efficient missions.

The goal of the BOUNDARY-Layer Transition (BOLT) program has been to improve high-speed boundary-layer transition models and increase prediction capabilities for flow over a geometry that introduces several transition mechanisms that may potentially interact.<sup>1</sup> To that end, two flight tests have been conducted. BOLT, now retroactively known as BOLT-1A, launched from the Esrange Space Center in June 2021,<sup>2–6</sup> and BOLT-II launched from the Wallops Flight Facility in March 2022.<sup>7–10</sup> Many ground tests<sup>11–18, 19–22</sup> and computational efforts<sup>23–32, 33–36</sup> supported the BOLT and BOLT-II flight tests through investigation of the flow physics on the BOLT geometry for  $M > 5$ .

The BOLT geometry has been tested extensively in ground test facilities with Mach 6 flow. A common, one-third-scale wind-tunnel model (of the 0.866-m long flight vehicle) was fabricated in 2018<sup>17</sup> and tested in the quiet tunnels at Purdue University and Texas A&M University (TAMU), as well as conventional tunnels at TAMU and NASA Langley Research Center.<sup>16</sup> The model was mostly aluminum, but one testing surface was machined out of polyether ether ketone (PEEK) to allow for infrared (IR) thermography. The model was instrumented with fast-response pressure transducers and Schmidt-Boelter heat-flux gauges. The surface heating distribution, visualized with the IR thermography, agreed well between the two quiet tunnels and with the computations.<sup>15</sup> Neither tunnel could attain a high enough quiet pressure at that time for boundary-layer transition to occur on the model. In noisy flow, the transition pattern was similar across the Purdue, TAMU, and Langley facilities. Turbulent wedges developed on both sides of a relatively cold midspan. Common spectral peaks were also observed in the pressure fluctuations, particularly for sensors located near the centerline. Conducting multiple experiments on a common model was not limited to wind tunnel testing. The actual BOLT-II test article was tested in the LENS II facility at CUBRC prior to launch.<sup>19</sup>

Measurements were also made on models designed with intentional steps between the nosetip and frustum<sup>12, 13</sup> to imitate steps that could potentially develop on the flight vehicle due to thermal expansion. Boundary-layer trips were studied<sup>20, 21, 33, 34</sup> since they were applied to one experimental surface on the BOLT-II flight vehicle to promote transition and larger areas of turbulent flow. A longer BOLT variation was also investigated since the BOLT-II flight testing article was originally expected to be longer than its final 1-m length.<sup>22, 35, 36</sup> More recently, other renditions of the geometry have varied the leading-edge curvature and flattened the testing surfaces.<sup>37</sup> The flat surfaces allow off-body optical measurements, like focused-schlieren imaging,<sup>38</sup> to be made on the model.

While the focus has been on testing in hypersonic facilities since that is the target flight regime, supersonic ground test data serve as a significant complement to the abundant Mach 6 measurements. Supersonic ground test data are important, particularly from a quiet facility, because the flight vehicle must necessarily pass through supersonic flow to reach the hypersonic condition. Additionally, the BOLT-1A flight vehicle reached a maximum Mach number of 3.9 during ascent and 2.8 on descent,<sup>3</sup> so only supersonic data are available for that particular test. The present experiment expands on the work of Davami et al.<sup>39</sup> to examine the BOLT geometry in supersonic ( $M = 3.5$ ) flow. Section II describes the tunnel and model geometry for the present test entry. The experimental methods are presented in section III. The results are shown in section IV, followed by a discussion in section V that relates the present results to previous experimental campaigns on BOLT. Section VI closes out the paper with some conclusions.

## II. Facility and Model

### A. The Supersonic Low Disturbance Tunnel

The NASA Langley Supersonic Low Disturbance Tunnel (SLDT) is a Mach 3.5 blowdown tunnel that can operate as a quiet or noisy facility with the nozzle bleed valves opened or closed, respectively.<sup>40</sup> The bleed slot is located at the nozzle throat, where suction allows the formation of a new laminar boundary layer. This delays boundary-layer transition on the contoured nozzle walls and extends the quiet core, which is commonly defined as the region of uniform flow where the pressure or mass-flux root-mean-square (rms) fluctuations are less than 0.1% of the mean value.<sup>41,42</sup> Two nozzle configurations are available for the SLDT, 2-D planar and axisymmetric. The rapid-expansion 2-D planar nozzle was used in the present test. The quiet core is in the shape of a rhombus in the  $X$ - $Y$  plane, bounded upstream by the start of uniform flow and downstream by significant acoustic disturbances radiated into the flow from the turbulent boundary layers on the nozzle.<sup>40</sup> The nozzle exit cross section is 15.24 x 25.40 cm. The tunnel air is supplied from common high-pressure bottle fields, and the vacuum is provided by large vacuum spheres that are evacuated by pumps and a steam ejector. The tunnel can generally run for hours at a time. More details on the shared infrastructure are found in Berger et al.<sup>43</sup>

The nominal total temperature was 299.8 K (80 °F) for all tests, and the total pressure was swept from 82.7 to 276 kPa (12 to 40 psia) for the IR measurements of the model surface. Freestream hot-wire surveys were taken at fixed total pressure values of 138, 207, and 276 kPa, and off-body measurements were made for  $p_{01} = 138$  kPa. Sutherland's Law was used to compute viscosity. The testing conditions are summarized in Table 1.

Table 1. Nominal testing conditions.

	Surface	Freestream	Off-body
$M$	3.5	3.5	3.5
$T_0$ (K)	299.8	299.8	299.8
$p_{01}$ (kPa)	82.7 – 276	138, 207, 276	138
$Re \times 10^{-6}$ ( $m^{-1}$ )	4.75 – 15.8	7.92, 11.9, 15.8	7.92

### B. BOLT Model

The BOLT geometry is characterized by a blunted nosetip that branches into four swept leading edges that are connected by concave surfaces. Low-curvature testing surfaces are separated from each other by the higher-curvature “gutter” surfaces. The present BOLT model is a 30% scale model of the flight vehicle (90% of the commonly tested one-third-scale models). This was the largest size that could fit within the facility without impact from a reflected shock wave. The model was 3-D printed of polycarbonate in 2 pieces, with the seam located at  $x/L = 0.213$ , the same relative position as the interface between the stainless steel nosetip and aluminum frustum on the flight vehicle. The nosetip was aligned to the frustum using dowel pins and secured with epoxy. The model frustum was printed with an interior cavity for an aluminum strongback mount. The mount was secured to a 25.4-mm (1-in.) diameter sting that was held by a strut fastened to the floor of the test section. Top and isometric views of the model are shown in Fig. 1.

Fiducial markers were applied to various locations near the aft end of the model to map the 2-D IR images to body-fixed coordinates. The markers were retroreflective, with a low emissivity compared to the plastic model. The markers were only  $20 \pm 5$   $\mu m$  thick and were applied a sufficient distance downstream of the leading edge to avoid tripping the boundary layer. The markers had a diameter of 2 mm, which was large enough for identification in the IR images. The upper (Side A) and lower (Side B) testing surfaces of the model had 11 and 14 markers, respectively.

The surface was scanned for roughness and imperfections using a 3-D optical profilometer and was also scanned with a blue-light 3-D scanner for comparison with the designed geometry and to precisely measure the position of each fiducial marker.

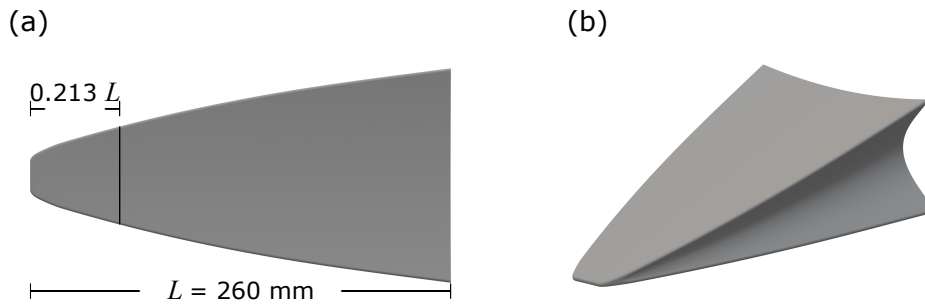


Figure 1. The BOLT wind-tunnel model: (a) top and (b) isometric views.

### 1. Optical Scans

Both test surfaces of the model were scanned using a 3-D optical profilometer before and after improving the model surface quality. The improvements consisted of sanding the model to reduce the surface roughness, largely due to the printing layers, and filling gaps between the nosetip and the frustum. These gaps were most significant on the leading edges of the model since both the nosetip and the frustum had some rounding due to the printing process. Therefore, particular emphasis was placed on the nosetip and interface regions when conducting the scans. Optical maps of scans on Side A of the as-printed model are shown in Fig. 2 (a–c) and of the improved model in Fig. 2 (d–f). Significant gaps are observed on the leading edges between the mating surfaces on the  $-z$  and  $+z$  sides of the model in (a) and (c), respectively. Each gap is in the shape of a wedge that becomes wider and deeper farther outboard. The gap distance along the leading edge is estimated as  $480\ \mu\text{m}$  on the  $-z$  side and  $570\ \mu\text{m}$  on the  $+z$  side. The interface across the span is not shown here, but the step was minimal on both testing surfaces of the model at less than  $20\ \mu\text{m}$ . There was, however, a gap between the nosetip and frustum that was consistently  $350\ \mu\text{m}$  across the span with an average depth of  $60\ \mu\text{m}$ . The model was printed in layers normal to its base, and surface roughness due to the layers is readily observed in Fig. 2(b) as vertical, i.e., spanwise-oriented, lines. This scan is from the central portion of the model nosetip. The periodicity of the roughness is further described in the following subsection.

A second set of scans were performed after the gap at the interface was filled and the model was sanded. Though artifacts of the gap still appear in Fig. 2 (d) and (f), the interface is now smooth to the touch. The optical measurements suggest that the maximum step height between the printed surfaces and the fill is less than  $20\ \mu\text{m}$  throughout both regions. Significant differences are also observed for the tip of the model, shown in Fig. 2(e). The printing lines were nearly eliminated, but the curvature was also altered. The differences in nosetip curvature can be more readily interpreted from Fig. 3(a). This plot shows the relative height, averaged across the span, as a function of relative streamwise distance. The downstream portion of the curves was leveled in the plot to facilitate better comparison. The original scans on Side A and Side B, are consistent with each other and show the front face of the tip transitioning at high curvature to a full height profile. Interestingly, the relative height is actually higher immediately following the curvature than it is farther downstream, which is likely an error associated with the printing. The sanded scans are also remarkably consistent between the two test surfaces and show a more gradual transition from the front face to the upper surface of the nosetip.

### 2. Surface Roughness

The data from the nosetip scans on both models, shown in Fig. 3(a), are shown again in Fig. 3(b), but offset in relative height to highlight the periodic nature of the roughness before sanding the model and its near elimination afterward. Spectral analysis of the individual as-printed streamwise-directed height profiles (not shown here) indicates a strong peak at a wavelength of  $100\ \mu\text{m}$ , with no other wavelengths significant. This wavelength is consistent with a printing-layer thickness of  $100\ \mu\text{m}$ . The rms roughness height was computed as  $R_q = 6.98\ \mu\text{m}$  using a cutoff wavelength and sampling length of  $800\ \mu\text{m}$ . A similar analysis was performed on the scan of the sanded model. The highest amplitude wavelength in the power spectral density (PSD) was still near  $100\ \mu\text{m}$ , but the amplitude was reduced by more than two orders of magnitude. The rms surface roughness was  $R_q = 1.18\ \mu\text{m}$ . Close inspection of the images in Fig. 2 shows the leading edges are not particularly well resolved. This is due to surface curvature since the optical profilometer has difficulty measuring semi-transparent surfaces that are oblique relative to the detector. The roughness parameters along the leading edges are assumed to be similar to those measured on the lower-curvature surfaces.

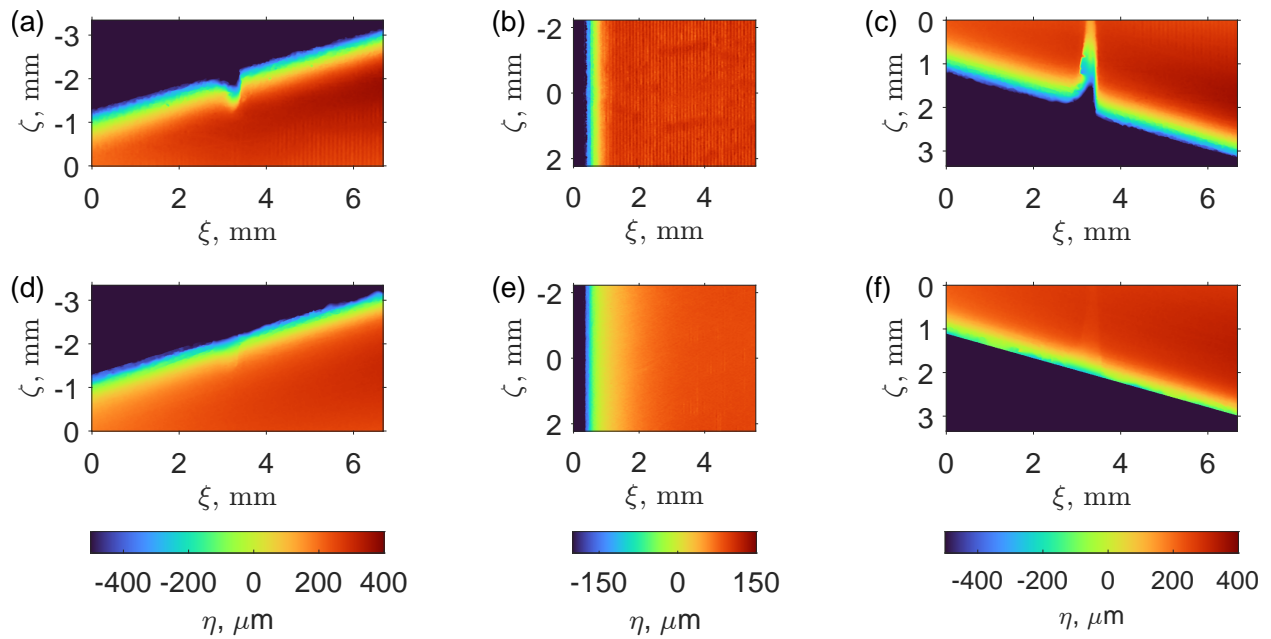


Figure 2. Relative height maps of important features on Side A. Scans (a–c) are of the as-printed model. (a) and (c) are of the leading edge gap on the  $-z$  and  $+z$  sides, respectively. Scan (b) is of an upstream portion of the nose, near the centerline. The same regions are shown in the lower row, scans (d–f), after improvements were made to the model.

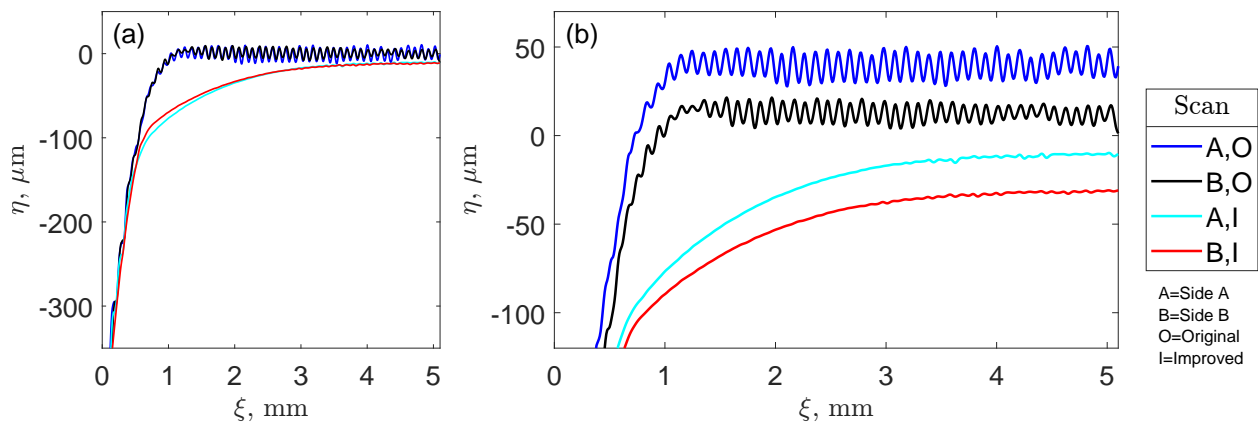


Figure 3. Relative height averaged across the span on the central nose regions of Side A and Side B before and after model improvements. (a) Scans are aligned to highlight differences in curvature. (b) Scans are offset to illustrate surface roughness.

### III. Experimental Methods

#### A. IR Thermography

Surface temperature measurements were acquired on the upper and lower surfaces of the model using two different long-wave (8–14  $\mu\text{m}$ ) IR cameras, which were mounted within the test section enclosure. The camera that was directed down at the upper experimental surface has a spatial resolution of 640 x 480 pixels and was sampled at 10 Hz. The camera directed up at the lower experimental surface has a spatial resolution of 160 x 120 pixels and was sampled at 8.7 Hz. Both cameras were calibrated with a black body radiation source prior to testing. The thermal properties of the polycarbonate are listed in Table 2. Emissivity was treated as a constant (0.94) regardless of viewing angle.

Two type-T thermocouples were also secured to the base of the model for direct comparison with the IR measure-

**Table 2. Thermal properties of polycarbonate.**

$c_p$ (J·kg <sup>-1</sup> ·K <sup>-1</sup> )	$\alpha$ (mm <sup>2</sup> ·s <sup>-1</sup> )	$\rho$ (kg·m <sup>-3</sup> )	$k$ (W·m <sup>-1</sup> ·K <sup>-1</sup> )	$\epsilon$
2880	0.0990	993	0.283	0.94

ments. The time series of the internal temperature distribution and surface heat-flux values were approximated using a 1-D heat conduction code based on QCALC.<sup>44</sup> The temperature values from the IR provided the upper boundary condition. A third type-T thermocouple was embedded approximately 12.7 mm (0.5 in.) within the base of the model to monitor the internal temperature of the model. This measurement supplied the interior boundary condition, set at a depth of 12.7 mm, which is a reasonable simplification for the portion of the model that was imaged, aside from the leading edges.

Each IR run followed the same general procedure, but there was some variation from run to run. A vacuum was pulled on the tunnel, and then the tunnel supply valves were opened to start the supersonic flow. The total pressure was quickly brought to  $p_{01} = 83$  kPa. At that point, the nozzle bleed valves were opened for quiet-flow runs. From there, the total pressure was ramped to 276 kPa, for a maximum  $Re = 15.8 \times 10^6 \text{ m}^{-1}$ . The rate of increase in total pressure was roughly constant within a given run and averaged  $3.12 \pm 1.14$  kPa/s over 29 different runs ( $R^2 = 0.9944$ ). Then, the pressure was ramped back down at a similar rate to  $p_{01} = 83$  kPa, where the bleed valves were closed and the tunnel was brought down to rest. Each tunnel run lasted approximately 5 minutes.

## B. Hot-wire Anemometry

Freestream hot-wire surveys were taken within the nozzle to approximate the freestream mass-flux fluctuation levels that the model would experience. The probe had a dual-wire configuration with 5.1- $\mu\text{m}$  diameter platinum-plated tungsten wires. The nominal length of the wires was 1.25 mm, and the spacing between them was 0.50 mm. The wires were spot welded to the prongs with slack to prevent effects from strain gauging. The wire overheat was set to 0.75, making the wire primarily sensitive to mass-flux fluctuations. The wires were calibrated at  $(X, Y, Z) = (152.4, 0, 0)$  mm for  $p_{01} = 103 - 310$  kPa (15 - 45 psia), in 34 kPa (5 psi) increments. Freestream surveys were then acquired for unit Reynolds numbers of  $7.92 \times 10^6 \text{ m}^{-1}$ ,  $11.9 \times 10^6 \text{ m}^{-1}$ , and  $15.8 \times 10^6 \text{ m}^{-1}$  ( $p_{01} = 20, 30, 40$  psia). The volume of measurements was bounded by  $X : [152.4, 355.6]$  mm,  $Y : [-38.1, 38.1]$  mm, and  $Z : [-63.5, 63.5]$  mm. The resolution was 25.4 mm in  $X$  and 12.7 mm in  $Y$  and  $Z$ .

When measurements on the model were conducted, the model was centered at  $(Y, Z) = (0.3, 4.2)$  mm. Four different streamwise positions were tested, with the nose positioned at  $X = 158.5, 183.9, 209.3,$  or  $234.7$  mm. A top view of these four model positions relative to the nozzle, represented by the black dashed line, is shown in Fig. 4(a). Model positions 1 to 4 (P1-P4) increment with downstream position and are depicted using increasingly dark shades of gray. A contour of rms mass-flux fluctuation levels for the  $X-Z$  plane at  $Y = 0$  and  $Re = 11.9 \times 10^6 \text{ m}^{-1}$  is also shown in the figure. The contour lines represent  $2.5 \times 10^{-4}$  increments in the normalized mass-flux fluctuations. Fluctuation levels below the quiet threshold  $(\rho u)' / (\rho u) < 10^{-3}$  are shown as dark violet. Values above  $5 \times 10^{-3}$  are dark red. The figure shows that the quiet core converges toward the centerline with increasing streamwise distance as noise radiates from the sidewall boundary layers. This is similar to the effect that occurs in the  $X-Y$  plane, where noise radiates into the flow from the contoured walls.

Since the entire model did not fit in the quiet core, the freestream noise levels projected to the leading edge of the upper surface of the model were estimated for the four streamwise positions of the model, (P1-P4). These normalized mass-flux fluctuation levels are shown in Fig. 4 (b-d) for unit Reynolds numbers of  $7.92 \times 10^6 \text{ m}^{-1}$ ,  $11.9 \times 10^6 \text{ m}^{-1}$ , and  $15.8 \times 10^6 \text{ m}^{-1}$ , respectively. The downstream portions of model edges shown in gray are located farther downstream than the bounds of the freestream survey. Note that the noise levels in Fig. 4(c) are similar, but not identical, to those in Fig. 4(a) since the leading edge is increasingly offset from  $y = 0$  farther downstream. Due to the spanwise model positioning, higher levels of noise hit the  $+z$  side of the model at a given  $X$ . For example, with the model at P1, given  $X = 300$  mm, the fluctuations are  $2.0 \times 10^{-3}$  on the  $+z$  side and  $1.5 \times 10^{-3}$  on the  $-z$  side. The effect of the freestream noise difference at the leading edges on the transition front is observed in the IR images in Section IV.

Similar freestream measurements were made for the same unit Reynolds numbers in noisy flow. The noise levels for the “bleeds-closed” configuration are shown in Fig. 5. The fluctuation distribution for the  $X-Z$  plane at  $Y = 0$  and  $Re = 11.9 \times 10^6 \text{ m}^{-1}$  in Fig. 5(a) is markedly different from the quiet case. For the noisy case, quiet flow is observed up to  $X = 183$  mm, where it abruptly ends across the span. From there, the normalized rms mass-flux fluctuations

increase to  $5.0 \times 10^{-3}$  by  $X = 220$  mm. Farther downstream, the fluctuation levels are generally near or above  $5.0 \times 10^{-3}$ . As a result, only the very tip of the model is situated inside the quiet core for even the farthest upstream P1 model position. The normalized mass-flux fluctuation levels along the model leading edge are again shown in Fig. 5 (b–d) for unit Reynolds numbers of  $7.92 \times 10^6 \text{ m}^{-1}$ ,  $11.9 \times 10^6 \text{ m}^{-1}$ , and  $15.8 \times 10^6 \text{ m}^{-1}$ , respectively. The fluctuations are relatively high over the bulk of the model regardless of freestream Reynolds number.

Off-body measurements were acquired above Side A using a custom-made “blade” probe that was designed to minimize intrusion to the boundary layer. The blade probes were investigated at the same time as the wedge probes that are reported in Owens et al.<sup>45</sup> The wire on the present blade probe was a 3.8- $\mu\text{m}$  diameter platinum-rhodium (90Pt-10Rh) wire. The nominal length of the wire was 0.5 mm, and it was also spot welded to the prongs. The wire overheat was again set to 0.75. A  $y$ - $z$  plane was surveyed with the hot-wire anemometer near the base of the model at  $x = 257$  mm ( $x/L = 0.99$ ). The plane consisted of a  $37 \times 27$  ( $z \times y$ ) point grid, centered on the span and extended to  $z = \pm 7.20$  mm. Measurements were bounded by  $y = 0.60$  mm and  $y = 4.44$  mm, where  $y = 0$  was the local vertical coordinate at  $z = 0$ . Cold-wire resistance measurements were also made at each location on the survey to correct for total temperature variation across the plane. Additional details on the hot-wire data processing methods, including the iterative steps required to correct for differences in total temperature through the boundary layer, are explained in Kegerise et al.<sup>46</sup> The measured mean and two-standard-deviation tunnel conditions for the points acquired in each survey are listed in Table 3. Note that the standard deviation values are listed to demonstrate the stability of the conditions within a given survey and do not account for instrumentation uncertainty.

**Table 3. Summary of hot-wire survey conditions.**

Type	Flow	$\bar{p}_{01}$ (kPa)	$2 \cdot \sigma_{\bar{p}_{01}}$ (kPa)	$\bar{T}_0$ (K)	$2 \cdot \sigma_{\bar{T}_0}$ (K)
Freestream	Quiet	138.89	0.78	299.71	0.32
Freestream	Quiet	205.38	0.67	299.53	0.37
Freestream	Quiet	276.32	0.91	299.69	0.47
Freestream	Noisy	137.73	0.60	299.44	0.15
Freestream	Noisy	206.07	0.49	299.52	0.14
Freestream	Noisy	274.69	1.58	299.46	0.47
Off-body	Quiet	137.28	0.97	299.72	0.22

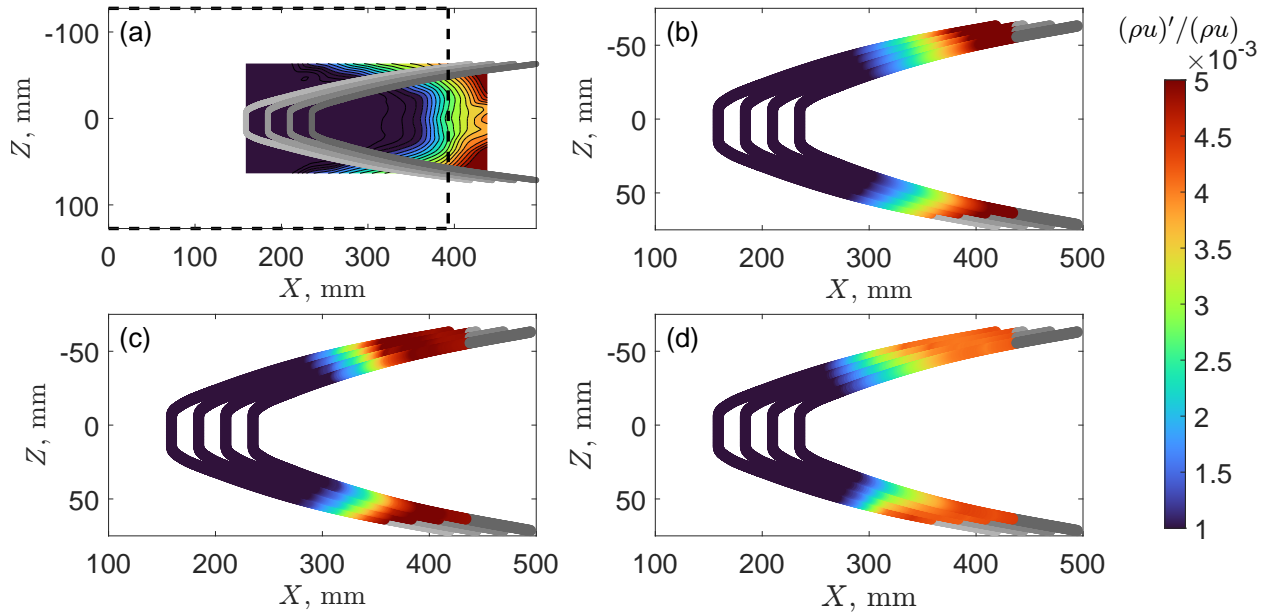


**Figure 4.** Freestream mass-flux fluctuations in quiet flow. (a) The four model positions within the nozzle and the normalized mass-flux fluctuations for the plane  $Y = 0$  at  $Re = 11.9 \times 10^6 \text{ m}^{-1}$ . The projected mass-flux fluctuations at the leading edge of the model for (b)  $Re = 7.92 \times 10^6 \text{ m}^{-1}$ , (c)  $Re = 11.9 \times 10^6 \text{ m}^{-1}$ , and (d)  $Re = 15.8 \times 10^6 \text{ m}^{-1}$ .

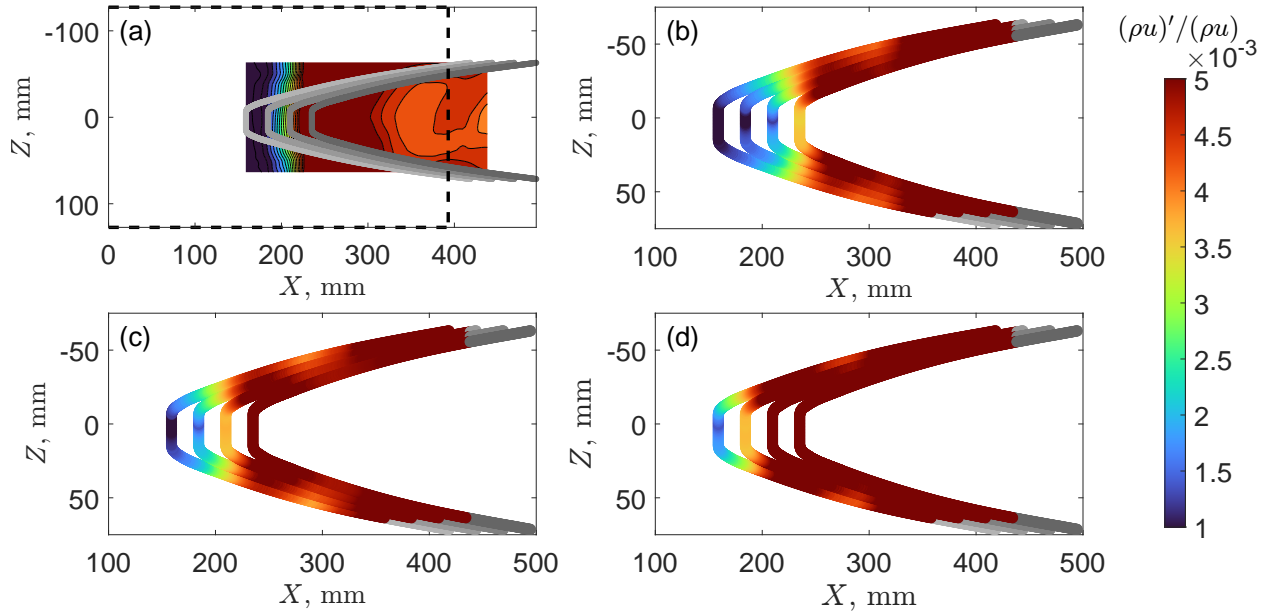


**Figure 5.** Freestream mass-flux fluctuations in noisy flow. (a) The four model positions within the nozzle and the normalized mass-flux fluctuations for the plane  $Y = 0$  at  $Re = 11.9 \times 10^6 \text{ m}^{-1}$ . The projected mass-flux fluctuations at the leading edge of the model for (b)  $Re = 7.92 \times 10^6 \text{ m}^{-1}$ , (c)  $Re = 11.9 \times 10^6 \text{ m}^{-1}$ , and (d)  $Re = 15.8 \times 10^6 \text{ m}^{-1}$ .

### C. Uncertainty Considerations

The measurement uncertainty related to the freestream conditions is based on the instrumentation uncertainty in total pressure and total temperature, which are  $\pm 110 \text{ Pa}$  and  $\pm 2.2 \text{ }^\circ\text{C}$ , respectively. These uncertainty values combined with the  $2\text{-}\sigma$  uncertainty in testing conditions and a  $\pm 0.02$  uncertainty in Mach number, results in a  $0.45 \times 10^6 \text{ m}^{-1}$

uncertainty for each documented unit Reynolds number.

There is substantially more uncertainty involved in computing the surface heat-flux values. The stated uncertainty in surface temperature for the primary Side A camera was  $\pm 2$  °C. The IR measurements were monitored for inconsistencies using surface thermocouples that were visible in the IR images. The uncertainty of the type-T thermocouples is  $\pm 1$  °C. These uncertainty values alone are relatively large compared to the difference between initial and adiabatic wall temperatures. Therefore, temperatures relative to initially measured values, rather than absolute temperatures, were used in the heat-flux calculations to reduce uncertainty due to offset. An initial series of frames acquired while the tunnel was under vacuum was averaged and then was subtracted from each frame during the run. Similarly, the initial thermocouple temperatures were subtracted from each respective thermocouple time series. This process, however, does not correct for drift that can occur when IR cameras are sampled for long durations.

Considering multiple runs introduces additional uncertainty in heat-flux values at a given freestream condition. The surface temperature values, the internal temperature distribution, and the resulting heat flux are all path dependent. The initial temperature is a critical parameter when estimating the heat flux. In this case, with the adiabatic wall temperature less than the initial wall temperature, a higher initial temperature results in a lower, i.e., more negative, distribution of heat-flux values if all other run conditions could be perfectly replicated. The average internal temperature over 29 runs was  $292.27 \pm 2.12$  K, while a surface thermocouple on the base of the model was generally slightly warmer, measuring  $292.50 \pm 2.40$  K. Each run was conducted at least 30 minutes following the previous run in an effort to promote temperature uniformity throughout the model. Offsets in initial temperature existed primarily due to differences in overnight temperature. Since the IR runs were only a few minutes long, the total temperature showed considerably more variation than was measured during the hot-wire runs. There was a positive correlation ( $R^2 = 0.7181$ ) between temperature and total pressure for the upward pressure ramp, with an average slope of  $0.0132 \pm 0.0182$  K/kPa. The average temperatures at  $p_{01} = 103.4$  kPa and  $262.0$  kPa were  $299.42 \pm 2.65$  K and  $301.35 \pm 1.84$  K, respectively.

## IV. Experimental Results

### A. IR Thermography

#### 1. Preliminary Considerations

IR images were acquired on both sides of the model, but only the results from the higher resolution camera directed at Side A are shown herein. The results from Side B are consistent with those from Side A. Both cameras were used throughout the campaign to verify that the pitch and yaw angles were near zero by comparison of the transition fronts. Additionally, only results from the increasing pressure portion of each run are shown because the features are more distinct in the heat-flux maps, and there are fewer artifacts from previous conditions.

Heat flux is the primary heat transfer parameter presented in this work. The values are generally negative since the adiabatic wall temperature over the entire surface was less than the initial wall temperature. While many previous BOLT campaigns reduced the heat transfer to an approximated Stanton number, that was not done herein since the calculation would introduce considerable additional uncertainty; the normalizing temperature difference,  $T_0 - T_w$ , is more than an order of magnitude smaller in the present test compared to the Mach 6 tests. Reducing to Stanton number does not provide an opportunity for similarity in this case due to the magnified impact of using  $T_0$ , rather than the conventional  $T_{aw}$ , for the normalization. Additionally, some examples of heat-flux minima would be further amplified, rather than moderated, by the normalization since the minima occur after the transition front passes over the location. Therefore, the normalization would be by a smaller temperature difference since the surface was just heated by the transition front. This was never an issue for the Mach 6 tests, in which the flow continually heated the model surface, and the heat flux at the transition front was not distinct from that of turbulent flow downstream of the front.

Features indicative of boundary-layer transition are identified below as areas of higher heat flux. An exception is the midspan, which will be described later. With the total temperature and model temperature near 300 K and 293 K, respectively, the recovery temperature for both laminar and turbulent boundary layers is below the model wall temperature. Since the laminar recovery temperature is lower than the turbulent recovery temperature, the temperature below the laminar boundary layer tends to decrease more rapidly toward its adiabatic state. Therefore, the heat flux with a laminar boundary layer generally has a more negative amplitude, i.e., more heat is convected away from the surface with a laminar boundary layer in this particular campaign.

## 2. Quiet Flow

The surface heat transfer maps for the as-printed model at streamwise station P2 for four different unit Reynolds numbers in quiet flow are shown in Fig. 6. The  $Re = 7.5 \times 10^6 \text{ m}^{-1}$  heat-flux distribution in Fig. 6(a) looks symmetric, with only slight differences in the streaks near  $z = \pm 25 \text{ mm}$ . All of the heat-flux values are negative, with the model cooling down toward its adiabatic wall temperature. The centerline region is cooling at the slowest rate, and that rate is brought closer to zero downstream as the span of the centerline region contracts. Significant asymmetries start to appear in Fig. 6(b) at  $Re = 10.0 \times 10^6 \text{ m}^{-1}$ , where a transitional wedge, identified by its higher heating levels, appears near the shoulder on the  $+z$  side. This feature is found to be the result of model positioning within the nozzle. The model is centered at  $Z = 4.2 \text{ mm}$ , which subjects the  $+z$  leading edge to higher freestream noise levels than the  $-z$ -side leading edge as shown in Section III.B. Asymmetric shoulder wedges are also observed on Side B (not shown here) for the same reason. The heat-flux distribution closer to the centerline is more symmetric. Transitional streaks are observed near the base on both sides of the centerline. These streaks curve slightly outboard as they advance upstream, with the  $-z$ -side streak slightly farther advanced. Outboard of those streaks, there are two more sets of transitional fingers originating at the base on each side near  $z = \pm 15$  and  $\pm 27 \text{ mm}$ . The transition front is far more asymmetric in Fig. 6(c) at  $Re = 12.5 \times 10^6 \text{ m}^{-1}$ . The full transition front is established on the  $+z$  side, while it is still undefined between  $z = -40$  to  $-50 \text{ mm}$  on the  $-z$  side. The transition front is farther advanced across the entirety of the  $+z$  side, compared to the  $-z$  side, including near the centerline. Similar observations are made from Fig. 6(d) at  $Re = 15.0 \times 10^6 \text{ m}^{-1}$ . The transition front is established across the model span but is farther advanced on the  $+z$  side. Moving inboard from the shoulder transition advancement, the  $+z$  side transition front constantly advances upstream until the centerline. This is not the case on the  $-z$  side, where the transition front appears more jagged, with a local upstream advancement near  $z = -33 \text{ mm}$  that falls back downstream before advancing again closer to the centerline.

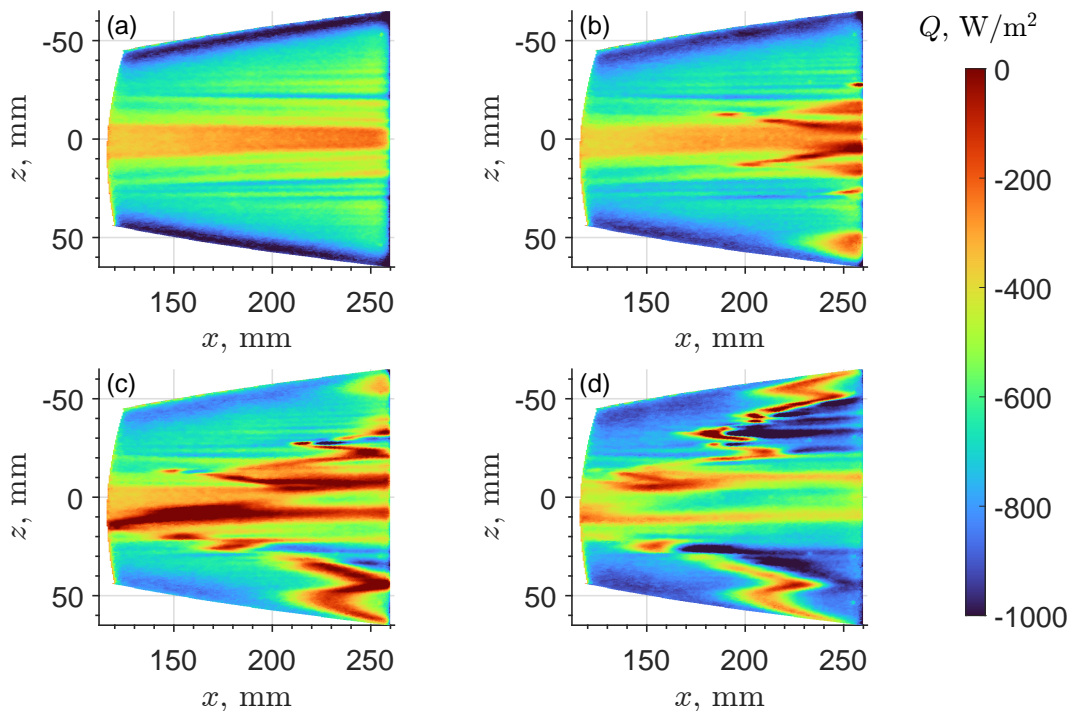


**Figure 6. Surface heat-flux values before model improvements in quiet flow for (a)  $Re = 7.5 \times 10^6 \text{ m}^{-1}$ , (b)  $Re = 10.0 \times 10^6 \text{ m}^{-1}$ , (c)  $Re = 12.5 \times 10^6 \text{ m}^{-1}$ , and (d)  $Re = 15.0 \times 10^6 \text{ m}^{-1}$ . The model was positioned at P2 ( $X = 183.9 \text{ mm}$ ).**

The surface heat transfer maps for the improved model at P2 for four different unit Reynolds numbers in quiet flow are shown in Fig. 7. The model improvements made a significant difference on the heat-flux distribution. The lowest  $Re$  map in Fig. 7(a) is similar to that of the as-printed model, except it appears to have fewer, or less distinct, streaks between the centerline and the shoulder. The  $Re = 10.0 \times 10^6 \text{ m}^{-1}$  heat-flux map in Fig. 7(b) appears somewhat similar to the  $Re = 7.5 \times 10^6 \text{ m}^{-1}$  heat-flux map in Fig. 6(a), with well-defined streaks on both sides of the centerline. The same noise-induced wedge appears on the  $+z$ -side shoulder in both the as-printed and improved  $Re = 10.0 \times 10^6$

$\text{m}^{-1}$  heat-flux maps. A transition wedge just outboard of the centerline is also established on the  $+z$  side in Fig. 7(b). The heat-flux distribution in Fig. 7(c) is quite symmetric, especially compared to that of the as-printed model. The transition fronts on the shoulders are qualitatively similar for both runs, but the remainder of the transition front on the  $+z$  side shows the starkest contrast. The only notable advancement is a wedge-shaped front, centered at  $z = 29$  mm. Transition is minimal between that wedge and the near-centerline transitional streaks. The transition front on the  $-z$  side at  $z = -29$  mm is located farther downstream on the improved model but is comparable in shape to that of the as-printed model. Similar observations of the transition front are made for Fig. 7(d). It is fairly symmetric about the centerline, aside from the shoulder wedges. Advances are observed near the centerline around  $z = \pm 6$  mm and farther outboard near  $z = \pm 29$  mm.

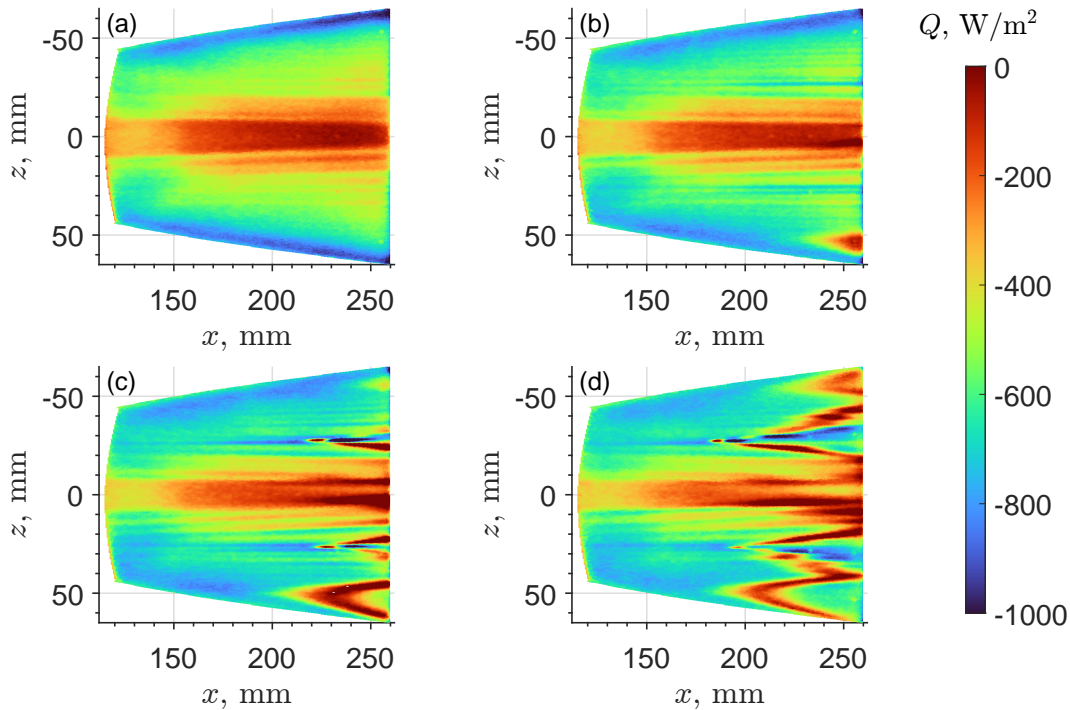


**Figure 7. Surface heat-flux values after model improvements in quiet flow for (a)  $Re = 7.5 \times 10^6 \text{ m}^{-1}$ , (b)  $Re = 10.0 \times 10^6 \text{ m}^{-1}$ , (c)  $Re = 12.5 \times 10^6 \text{ m}^{-1}$ , and (d)  $Re = 15.0 \times 10^6 \text{ m}^{-1}$ . The model was positioned at P2 ( $X = 183.9$  mm).**

Further comparison between the as-printed and improved versions of the model tested in quiet flow are shown in Fig. 8. This figure shows the heat-flux values across the span at  $x = 220$  mm for different unit Reynolds numbers between  $5.0 \times 10^6 \text{ m}^{-1}$  and  $10.5 \times 10^6 \text{ m}^{-1}$ . Heat-flux distributions for both the as-printed model, in Fig. 8(a), and the improved model, in Fig. 8(b), show strong symmetry about the midspan. The laminar streak features from the IR images are local maxima in the present figure. The lower Reynolds number curves in both plots are similar, with a maximum value plateau across the centerline and a gradual ramping down in heat-flux farther outboard. The heat-flux slope steepens for  $|z| > 50$  mm, but this could be caused by the divergence from the uniform thickness approximation in the calculations. As the unit Reynolds number increases, the general distribution shape is the same, but additional and stronger streamwise streaks emerge, indicating an increase in waviness. Transitional features, detected as positive excursions from the general distribution, are noted near the centerline for the as-printed model in Fig. 8(a). The first instance is near  $z = -12$  mm for  $Re = 9.0 \times 10^6 \text{ m}^{-1}$ . Wedges appear on both sides of the centerline for  $Re = 9.5 \times 10^6 \text{ m}^{-1}$  and generally increase in magnitude and move toward the centerline as  $Re$  increases. The only feature of note for the improved model in Fig. 8(b) is from the transition wedge on the  $+z$ -side shoulder, observed near  $z = 51$  mm for  $Re = 10.5 \times 10^6 \text{ m}^{-1}$ .

The heating distributions change dramatically for the higher unit Reynolds numbers, between  $11.0 \times 10^6 \text{ m}^{-1}$  and  $15.0 \times 10^6 \text{ m}^{-1}$ , shown in Fig. 9. There is less symmetry, even for the improved model. The heat-flux plateau across the centerline for the lower  $Re$  becomes a local minimum for the higher  $Re$ , between two transitional or turbulent streaks. The heating caused by transition on the shoulders due to tunnel noise is evident for  $z < -50$  and  $z > 42$  mm. The greatest difference between the lower and higher  $Re$  spanwise distributions is the increase in heat-flux variation between the shoulder features and the near centerline. Some local maxima and minima, e.g., at  $z = -32, -27,$  and  $26$

mm in Fig. 9(a), appear isolated, with no continuity to their development. This is primarily observed on the as-printed model, where the transition front rapidly evolves and advances upstream for  $Re$  between  $12.0 \times 10^6 \text{ m}^{-1}$  and  $15.0 \times 10^6 \text{ m}^{-1}$ , so the development cannot be properly visualized using  $0.5 \times 10^6 \text{ m}^{-1}$  unit Reynolds number increments. The maxima at  $z = \pm 27 \text{ mm}$  in Fig. 9(b) are caused by a sudden onset of the transition front, but the evolution is clearer. The maxima are followed by local minima for subsequent  $Re$ , at the same  $z$ , once the transition front has passed over  $x = 220 \text{ mm}$  and turbulent flow is established. The low heat-flux values are not only an effect of the lower heat transfer for turbulent flow compared to transitional flow but are also due to the prior elevated temperatures of the wall that was just heated by the transitional flow. The transition front has a triangular shape, so maxima develop on both sides of the original  $z = \pm 27 \text{ mm}$  peaks as  $Re$  increases.

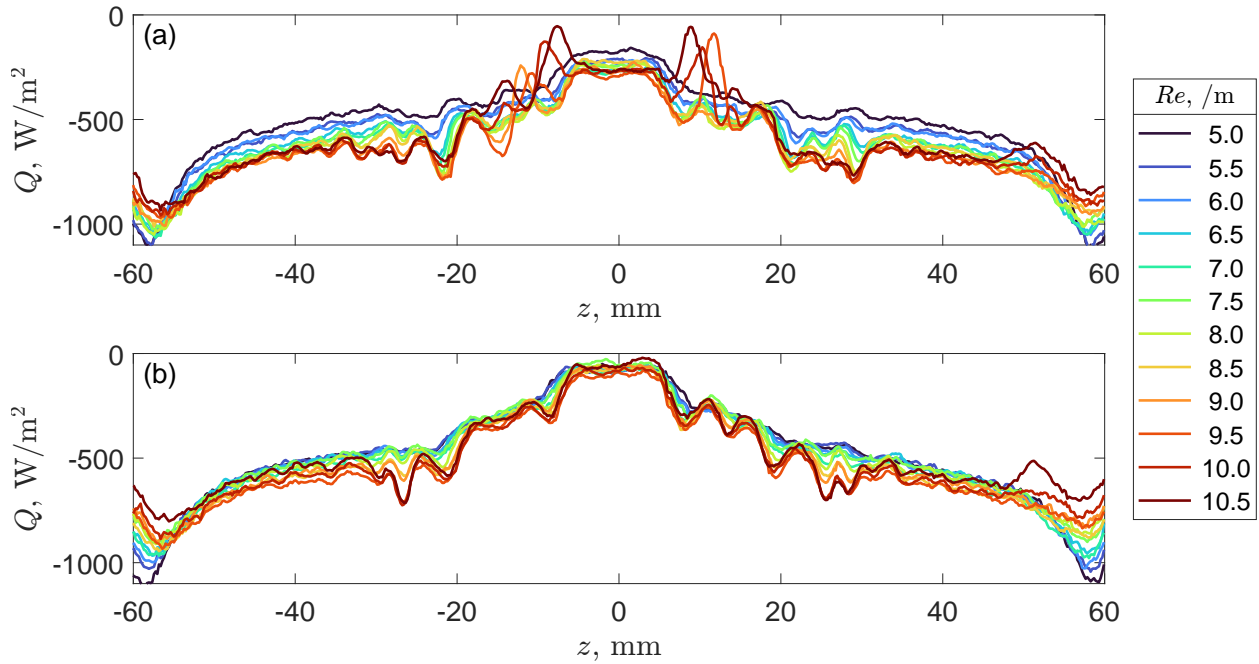


**Figure 8. Surface heat-flux values across the span at  $x = 220 \text{ mm}$  for  $5.0 \times 10^6 \leq Re \leq 10.5 \times 10^6$  for the (a) as-printed model and (b) improved model. The model was positioned at P2 ( $X = 183.9 \text{ mm}$ ) in quiet flow.**

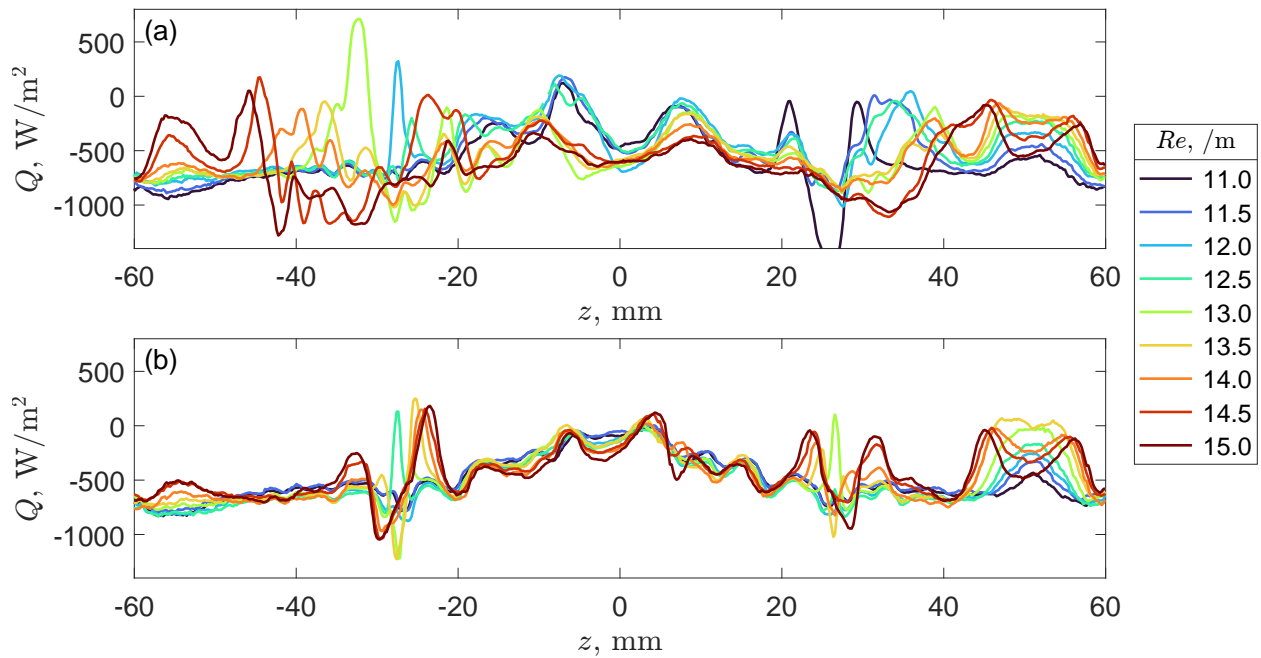


**Figure 9.** Surface heat-flux values across the span at  $x = 220$  mm for  $11.0 \times 10^6 \leq Re \leq 15.0 \times 10^6$  for the (a) as-printed model and (b) improved model. The model was positioned at P2 ( $X = 183.9$  mm) in quiet flow.

### 3. Noisy Flow

The heat-flux maps generated from runs conducted in noisy flow are very different compared to those from quiet flow. Maps of heat flux for four different unit Reynolds numbers for the as-printed model positioned at P2 are shown in Fig. 10. Transition is already observed in Fig. 10(a) for the lowest  $Re = 5.0 \times 10^6 \text{ m}^{-1}$  case, and the heating pattern is quite symmetric about the centerline. Transitional wedges are located on both shoulders. The shape and size of the wedges is similar to the wedge observed on the  $+z$  side shoulder for  $Re = 12.5 \times 10^6 \text{ m}^{-1}$  in quiet flow. The symmetry in noisy flow suggests that the noise levels are roughly equal on the  $+z$  and  $-z$  leading edges. Transitional streaks also appear near the base on either side of the centerline around  $z = \pm 4$  mm. The transition front advances considerably by  $Re = 7.5 \times 10^6 \text{ m}^{-1}$  in Fig. 10(b). Transition on the shoulders advances roughly 50 mm, to around  $x = 150$  mm and extends inboard to roughly  $z = \pm 20$  mm. The single transitional streaks that originate on either side of the centerline spread apart with increased  $Re$  and appear to bifurcate upstream near  $x = 210$  mm. The transition fronts for  $Re = 10.0 \times 10^6 \text{ m}^{-1}$  and  $Re = 12.5 \times 10^6 \text{ m}^{-1}$ , in Fig. 10(c) and (d), respectively, have similar defining characteristics and continue to advance farther upstream. Large swaths of turbulent flow are observed downstream of the transition fronts on the shoulders. The heat-flux values are significantly lower and more uniform in the regions of turbulent flow compared to values observed at the transition front.

The model improvements led to minor differences in the heat-flux maps for noisy flow. The image for  $Re = 5.0 \times 10^6 \text{ m}^{-1}$ , in Fig. 11(a), shows fewer streamwise streaks compared to the map for the as-printed model. The transition wedges on the shoulders are slightly smaller, and the transitional fingers near the centerline are less distinct. The greatest difference in the  $Re = 7.5 \times 10^6 \text{ m}^{-1}$  map, Fig. 11(b), involves the heating distribution near the centerline. In the corresponding as-printed model heating map, a single transitional streak appears to bifurcate upstream on both sides of the centerline. For the improved model, two transitional streaks appear on both sides of the centerline. An outboard set of streaks is located near the base of the model, and an inboard set of transitional streaks is located upstream, near  $x = 200$  mm. The transition front looks similar for  $Re = 10.0 \times 10^6 \text{ m}^{-1}$  in Fig. 11(c), except that the inboard portion of the shoulder transition fronts appear to merge with the aforementioned outboard near-centerline transitional streaks. A similar transition pattern pushes farther upstream for  $Re = 12.5 \times 10^6 \text{ m}^{-1}$  in Fig. 11(d).

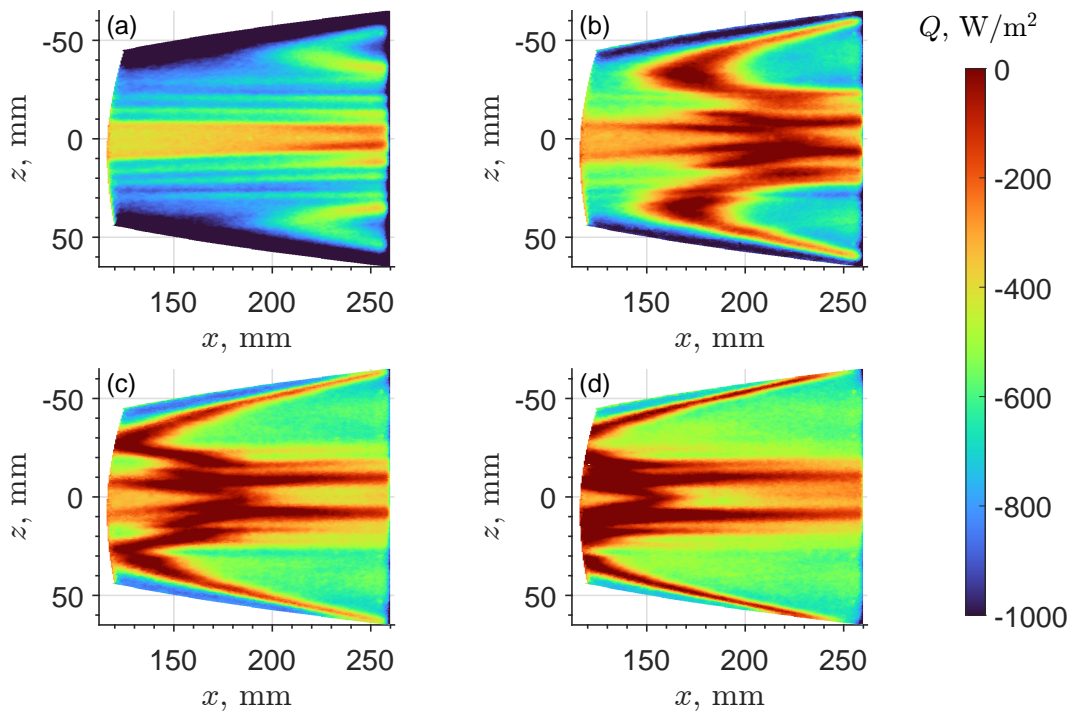


**Figure 10. Surface heat-flux values before model improvements in noisy flow for (a)  $Re = 5.0 \times 10^6 \text{ m}^{-1}$ , (b)  $Re = 7.5 \times 10^6 \text{ m}^{-1}$ , (c)  $Re = 10.0 \times 10^6 \text{ m}^{-1}$ , and (d)  $Re = 12.5 \times 10^6 \text{ m}^{-1}$ . The model was positioned at P2 ( $X = 183.9 \text{ mm}$ ).**

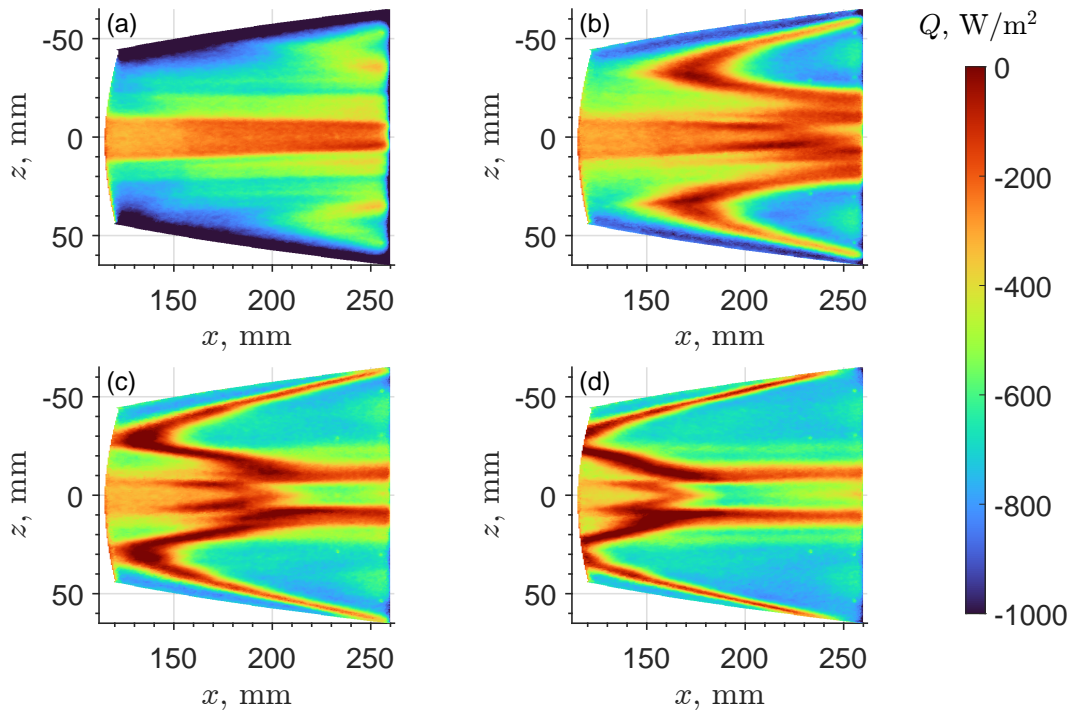


**Figure 11. Surface heat-flux values after model improvements in noisy flow for (a)  $Re = 5.0 \times 10^6 \text{ m}^{-1}$ , (b)  $Re = 7.5 \times 10^6 \text{ m}^{-1}$ , (c)  $Re = 10.0 \times 10^6 \text{ m}^{-1}$ , and (d)  $Re = 12.5 \times 10^6 \text{ m}^{-1}$ . The model was positioned at P2 ( $X = 183.9 \text{ mm}$ ).**

#### 4. Effect of Model Positioning

The influence of positioning within the nozzle on the surface heating of the improved model is shown in the heat-flux maps of Fig. 12. The top row of images, Fig. 12(a–c), are quiet runs at  $Re = 11.9 \times 10^6 \text{ m}^{-1}$  at streamwise stations P1, P2, and P3, respectively. With the model positioned farthest upstream at P1, more of the leading edge is exposed to quiet flow, and the result is minimal transitional near the base in Fig. 12(a). Transitional fingers are observed near  $z = \pm 4$  and small transitional wedges are centered near  $z = \pm 27 \text{ mm}$ . There is a hint of the noise-induced shoulder wedge on the  $+z$  side of the model. The heat-flux map for P2 is shown in Fig. 12(b). Minor advances are observed on the inboard transition fingers and wedges, but the transitional wedge on the  $+z$ -side shoulder is considerably more advanced. There are also the beginnings of a wedge on the  $-z$ -side shoulder. For P3, the transitional fingers closest to the centerline do not appear to advance farther upstream, and the streak on the  $-z$  side actually appears to be slightly weaker. However, the transitional wedges located between the centerline and shoulders advance slightly upstream, while the transition fronts on both shoulders advance significantly more.

The bottom row of images, Fig. 12(d–f), are heat-flux maps from the noisy runs at  $Re = 7.9 \times 10^6 \text{ m}^{-1}$  and streamwise stations P1, P2, and P3, respectively. The centerline transitional features and the shoulder transitional wedges are already prominent for P1 in Fig. 12(d). The shoulder transition fronts extend to roughly  $x = 170 \text{ mm}$ , while the centerline transitional streaks are slightly farther downstream, and they appear to be spread farther apart near the base. The shoulder transition fronts advance to near  $x = 150 \text{ mm}$  for P2 in Fig. 12(e). The transitional features near the centerline are similar to those in P1, but the inboard portions of the transition fronts from the shoulders encroach on the near-centerline features. Fig. 12(f) shows the heat-flux distribution for P3. The transition fronts for the shoulders continue to advance to  $x = 130 \text{ mm}$ , and the inboard portion of the shoulder transition front appears to merge with the centerline transitional features that are otherwise unchanged.

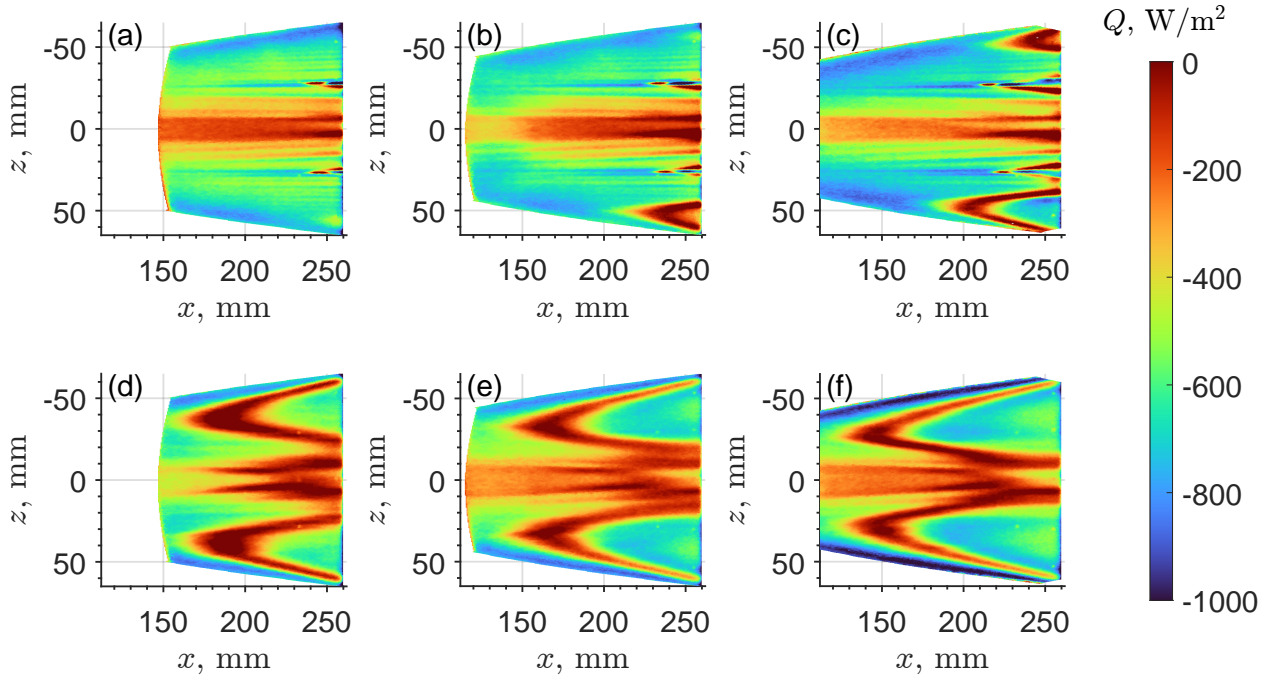


**Figure 12. Surface heat-flux values for the improved model at different streamwise positions in quiet and noisy conditions. Quiet runs (a–c) were conducted at  $Re = 11.9 \times 10^6 \text{ m}^{-1}$ . Noisy runs (d–f) were conducted at  $Re = 7.9 \times 10^6 \text{ m}^{-1}$ . Noretip positions within the nozzle are (a,d): P1 ( $X = 158.5 \text{ mm}$ ), (b,e): P2 ( $X = 183.9 \text{ mm}$ ), and (c,f): P3 ( $X = 209.3 \text{ mm}$ ).**

#### B. Off-body Measurements

Contour maps of the mean and fluctuating mass-flux values on the  $y$ - $z$  plane at  $x = 257 \text{ mm}$  are shown in Fig. 13. The model was positioned at P2 ( $X = 183.9 \text{ mm}$ ), and the quiet flow was at a unit Reynolds number of  $7.92 \times 10^6 \text{ m}^{-1}$ . The model surface is indicated by the thick, black curve near  $y = 0$ . The minimal curvature near the centerline, and limited span, render the surface as nearly flat. The white contour lines represent the mean mass flux, with the

bottom contour line of  $\rho u = 15 \text{ kg}\cdot\text{m}^{-2}\cdot\text{s}^{-1}$  increasing in increments of  $2.5 \text{ kg}\cdot\text{m}^{-2}\cdot\text{s}^{-1}$  to the top contour line of  $\rho u = 40 \text{ kg}\cdot\text{m}^{-2}\cdot\text{s}^{-1}$ . The present map does not encompass the entirety of the distorted mean flow since the freestream mass flux is  $47.4 \text{ kg}\cdot\text{m}^{-2}\cdot\text{s}^{-1}$ . The contours demonstrate reasonable symmetry about  $z = 0$ . Significant mean flow distortion is observed with a clear upwelling of lower momentum fluid near the centerline. Influence of the centerline-bounding vortices are also observed from the  $15 \text{ kg}\cdot\text{m}^{-2}\cdot\text{s}^{-1}$  contour, where an initial reduction in thickness is observed near  $z = \pm 4 \text{ mm}$  and a thickening from the rollup (clockwise rotation for  $+z$ ) is observed around  $z = 5 \text{ mm}$ . Higher momentum ( $>15 \text{ kg}\cdot\text{m}^{-2}\cdot\text{s}^{-1}$ ) fluid is observed closest to the wall for  $|z| > 6 \text{ mm}$ . At those same outboard span locations, and between 1–2 mm above the model surface, there is a large separation between the 22.5 and  $25 \text{ kg}\cdot\text{m}^{-2}\cdot\text{s}^{-1}$  contour lines, suggesting that the flow has relatively constant momentum beneath the crest of the vortices. Interestingly, the  $35 \text{ kg}\cdot\text{m}^{-2}\cdot\text{s}^{-1}$  contour is relatively flat across the span, balancing the distortion effects from the centerline and vortices. However, the  $40 \text{ kg}\cdot\text{m}^{-2}\cdot\text{s}^{-1}$  contour puts the greatest thickening at the center, trailing off toward the span. This contour and, correspondingly, the boundary-layer edge are expected to come even closer to the surface farther outboard, beyond the sampling range, and away from the influence of the centerline and its bounding vortices.

The filled contours represent the rms mass-flux fluctuations integrated from 100 Hz to 100 kHz, normalized by the mean mass flux. The fluctuation levels also demonstrate symmetry about  $z = 0$ , particularly the prominent vortices. The filled contour levels increase in 1.5-percent increments, from below 1.5% to below 18%. The normalized mass-flux values near the centerline are low, less than 1.5% for much of the area between  $z = \pm 2 \text{ mm}$ . The highest fluctuation levels are near  $z = \pm 6 \text{ mm}$  for the points measured closest to the wall. This region corresponds to an area of narrowly spaced mean contours, where the higher momentum fluid moves closest to the model surface. The vortex appears stronger on the  $+z$  side, as indicated by the slightly higher fluctuation levels (17.0% vs. 14.5%). A stronger vortex for  $+z$  is consistent with the earlier transition observed in this region of the IR image in Fig. 7(b) for the higher  $Re$  value of  $10.0 \times 10^6 \text{ m}^{-1}$ . Additional fluctuation maps (not shown here) were also examined using 10 kHz integration ranges between the overall 100 Hz to 100 kHz bounds. Each map looked qualitatively similar, with lower fluctuation levels observed for each subsequent 5 kHz frequency range. This suggests that the content is relatively broadband but is more heavily weighted toward lower frequencies.

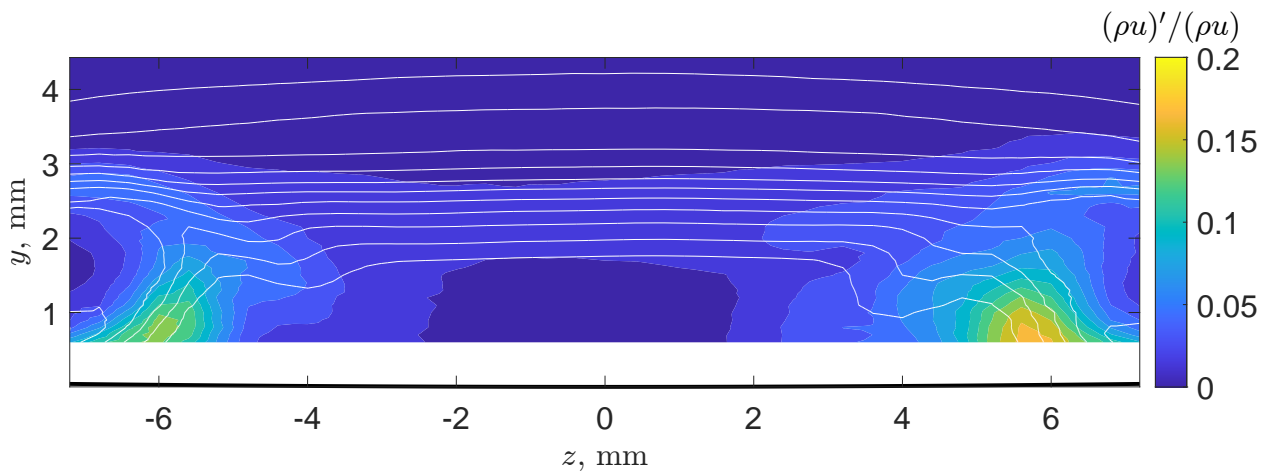


**Figure 13. Contour maps of mean mass flux and normalized rms mass-flux fluctuation above Side A at  $x = 257 \text{ mm}$  for  $Re = 7.92 \times 10^6 \text{ m}^{-1}$  quiet flow. The mean mass-flux contours are white lines in  $2.5 \text{ kg}\cdot\text{m}^{-2}\cdot\text{s}^{-1}$  increments. The fluctuations are represented by the filled contours that increment in 0.015 steps. The model surface is represented by the black curve near the bottom of the plot.**

Further investigation of the mass-flux fluctuation spectra was conducted. Power spectral density plots of the spectra, normalized by the mean mass flux, are shown in Fig. 14 for (a)  $z = 0$  and (b)  $z = 5.60 \text{ mm}$  at different heights above the model surface. Reference spectra from the aforementioned  $Re = 7.92 \times 10^6 \text{ m}^{-1}$  freestream survey are plotted for comparison. The gray, FS1 spectrum was acquired at roughly the same position as that of the off-body survey,  $(X, Y, Z) = (438.2, 38.1, 0) \text{ mm}$ . The black, FS2 spectrum was acquired around the location of the model nosetip at  $(X, Y, Z) = (184.2, 0, 0) \text{ mm}$ , which is well within the quiet core of the facility. The measured difference between these freestream spectra is more than an order of magnitude for frequencies out to 40 kHz, where  $f$ -squared anemometer noise,<sup>47</sup> rather than the flow physics, is responsible for the increase in the quiet-core spectrum. The

fluctuations are lower on the midspan than for  $z = 5.60$  mm, so the PSD scales differ between the two plots to better showcase the spectra. For  $z = 0$ , the spread between the spectra over the range in heights above the model is minimal. The PSD levels increase with increasing distance from the model surface, until  $y = 2.61$  mm, above which the spectra are approaching the edge of the boundary layer. The shape of the spectra changes slightly from a steady decline in magnitude over the frequency range for  $y = 0.6$  mm to a more broadband signal that extends out to 20 kHz for  $y = 1.8$  mm. The PSD amplitudes for all heights are well above the spectrum from the quiet core but are more comparable with FS1, especially for  $f > 5$  kHz.

The spectra from a profile that passes through the vortex are shown in Fig. 14(b). Here, the mean-normalized spectra decrease with increasing distance from the wall, with the  $y = 0.6$  mm spectrum having the highest PSD levels across the frequency range. The spectra fall off around  $f = 35$  kHz, and that fall-off frequency increases to 40 kHz for  $y = 1.80$  mm. A double peak is observed in the spectra for  $y = 2.15 - 3.22$  mm, with the lower-frequency peak centered near  $f = 17$  kHz, and the higher-frequency peak centered near 34 kHz. Further observation (not shown here) of spanwise-adjacent spectra indicates that  $y = 2.61$  mm is consistently where these peaks are most prominent. The spectral peaks increase in amplitude and decrease in frequency with increasing spanwise position from  $5.20 \leq z \leq 6.80$  mm, providing some insight to the dynamics of the vortex crest.

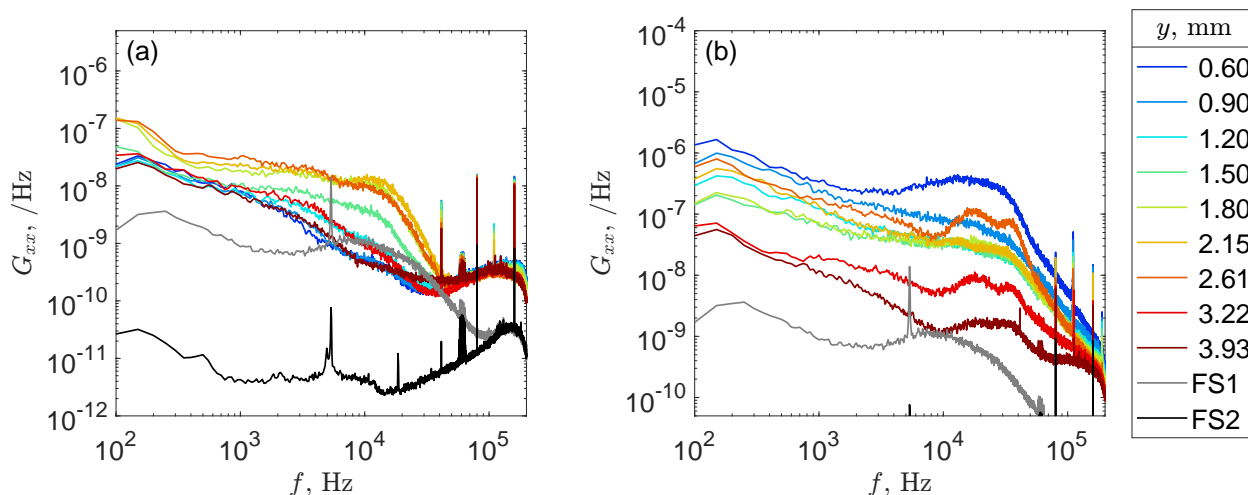


**Figure 14.** Power spectral density functions of normalized mass-flux fluctuations,  $(\rho u)'/(\rho u)$ , for  $y = 0.60 - 3.93$  mm above the model surface (a) at the midspan ( $z = 0$ ) and (b) through the vortex ( $z = 5.60$  mm). Freestream spectra, FS1 and FS2, are shown for comparison. The location of FS1 is near the planar survey, while FS2 is near the nosetip.

## V. Discussion

The results show some differences in comparison with the extensive Mach 6 ground tests. Although most of the Mach 6 ground tests were conducted in cold-flow facilities, the adiabatic wall temperature was always higher than that of the model surface. Therefore, the model temperature was always increasing, and the resulting heat flux was always positive across the surface. The TAMU wind tunnel tests are the best candidate for comparison since  $Re$  sweeps were also conducted to acquire those data. In the Texas A&M Mach 6 Quiet Tunnel, with  $T_0 = 430$  K and  $Re = 10.2 \times 10^6$   $m^{-1}$ , heat-flux values near the centerline were generally below  $1000$   $W \cdot m^{-2}$  and increased to roughly  $3000$   $W \cdot m^{-2}$  farther outboard.<sup>48</sup> The streamwise streak arrangement looks somewhat similar to those in Fig. 7(b). There are no published Mach 6 quiet tunnel results that show boundary-layer transition. Tests in noisy flow were conducted in the Actively Controlled Expansion tunnel. Turbulent wedges are observed on the shoulders for  $Re = 5.6 \times 10^6$   $m^{-1}$  and are shown to grow for  $Re = 8.0 \times 10^6$   $m^{-1}$ , but the wedges are the only transitional or turbulent features that are clear in the IR data. There were no transitional centerline streaks in the Mach 6 experiments, but there is some evidence of transition near the centerline based on pressure fluctuation spectra.<sup>15</sup> The heating distribution for the turbulent wedges on the shoulders is also different between the Mach regimes. The transition front at Mach 6 has generally been at the same heating level as the turbulent flow filling the wedge. The transition front at Mach 3.5 has been shown to have much higher heating than the turbulent flow that it bounds.

A major question from the IR imaging at Mach 3.5 is the cause of the relatively high heat flux on the centerline,

where values are negative but close to zero, while values for the rest of the map are generally much more negative. The off-body hot-wire survey conducted at  $Re = 7.92 \times 10^6 \text{ m}^{-1}$  demonstrates that the fluctuation levels are too low for the boundary layer to be transitional or turbulent, which is generally the cause of higher heating. Therefore, the higher, i.e., less negative, heating is due to the mean-flow distortion on the midspan, where an upwelling of lower-momentum fluid is observed, resulting in a thicker boundary layer. The heat flux at the wall is proportional to the temperature gradient, so the thicker boundary layer reduces the gradient and the resulting heat-flux magnitude at the wall. This reasoning is consistent with the Mach 6 results, where the thick boundary layer on the midspan mitigates the warming effect from the higher energy freestream.

Comparisons with the BOLT flight test are challenging due to the differences in testing conditions, model attitude, and the types of measurements acquired. Despite these differences, the flight data obtained during descent between  $t = 247 - 251 \text{ s}$  may be instructive for comparison. The Mach number was approximately 2.7, and the angle of attack oscillated but was mostly between  $4 - 8^\circ$ .<sup>3</sup> The centerline transitioned at  $x = 725 \text{ mm}$  for  $Re_L = 5.5 \times 10^6$ . For the present wind tunnel test, the centerline does not transition on the improved model tested in quiet flow for the highest  $Re_L = 3.9 \times 10^6$ , but transitional streaks do appear on either side of the centerline and toward the shoulder. Data from the flight experiment also indicate transition at lower Reynolds numbers for regions between the centerline and shoulder in comparison to the centerline. It is unclear if the transitional features possess a similar structure as those observed during the present wind tunnel campaign.

Given the significant difference that the model improvements made on the transition front, plans are in place to fabricate a solid model with lower surface roughness for additional off-body measurements. In the future, a separate run may need to be dedicated to each condition for the IR thermography to reduce uncertainty and minimize the artifacts that remain in the images from ramping through testing conditions. The consistency of the measurements could also be improved with a uniformly heated or cooled model.

## VI. Conclusions

In this study, measurements were made on a 30%-scale polycarbonate BOLT geometry in the Mach 3.5 Supersonic Low Disturbance Tunnel. The model was first tested as it was printed, with surface roughness due to the printing layers and leading-edge gaps where the nosetip was joined to the frustum. The model was improved by filling the gaps at the interface and sanding. Optical scans were made on the model to characterize the imperfections. Both versions of the model were tested in quiet flow and noisy flow and were tested at different streamwise positions within the nozzle. The entire model did not fit in the quiet core of the facility, so freestream hot-wire surveys were completed within the nozzle to approximate mass-flux fluctuation levels along the leading edge of the model.

Infrared thermography was the primary diagnostic used in this campaign. The surface temperature was monitored using two cameras and two thermocouples as the unit Reynolds number was swept from  $4.75 - 15.8 \times 10^6 \text{ m}^{-1}$ . A thermocouple was also embedded within the model to provide the internal boundary condition to approximate the heat flux. The total temperature and initial wall temperatures were near 300 K and 293 K, respectively, which generally resulted in heat transferring out from the model. Boundary-layer transition was observed on the model for every configuration, but there were significant differences in the heat-flux distributions between the different runs. Transition was not observed near the midspan on the improved model below  $10 \times 10^6 \text{ m}^{-1}$  in quiet flow, while it was already observed on the shoulders below  $5 \times 10^6 \text{ m}^{-1}$  in noisy flow. The transition front on the shoulders had much higher heat-flux levels than the downstream turbulent flow. This was not generally observed in previous Mach 6 studies, where the transition front and turbulent flow had similar heat-flux values. Also, transition in the Mach 6 conventional tunnels was dominated by the wedges on the shoulders of the model, and transition on the centerline was not observed. Positioning within the nozzle primarily made an impact on transition observed on the model shoulders. The difference in the shoulder heating was likely due to differences in freestream noise radiated from the nozzle sidewalls.

Hot-wire anemometry was also utilized to conduct a planar survey near the base of the model for the relatively low  $Re = 7.92 \times 10^6 \text{ m}^{-1}$  quiet condition. The survey demonstrated the thickening of the boundary layer near the centerline and the vortices on either side of it. The mass-flux fluctuations were as high as 17.0% within the vortices but were less than 2% above the midspan, suggesting that the boundary layer along the centerline is laminar. This allowed for the conclusion that the higher heat-flux levels observed near the centerline are not due to boundary-layer transition for the lower unit Reynolds number conditions.

## Acknowledgements

This work was supported by the Hypersonic Technologies Project under the NASA Aeronautics Research Mission Directorate. Operation of the NASA Langley SLDT facility was provided by Robert Edwards, C. David Gary, Rhonda Difulvio, Ricky Clark, and Danny Potthast. The fiducial marker position scans were performed by Kenneth Mcneil. Jonathan Davami is supported by a University of Notre Dame Dean's Fellowship and a NASA Pathways internship.

## References

- <sup>1</sup>Wheaton, B. M., Berridge, D. C., Wolf, T. D., Stevens, R. T., and McGrath, B. E., "Boundary Layer Transition (BOLT) Flight Experiment Overview," AIAA Paper 2018-2892, June 2018, <https://doi.org/10.2514/6.2018-2892>.
- <sup>2</sup>Wheaton, B. M., Butler, C. S., McKiernan, G. R., and Berridge, D. C., "Initial Results from the BOLT Flight Experiment," AIAA Paper 2022-0345, January 2022, <https://doi.org/10.2514/6.2022-0345>.
- <sup>3</sup>Butler, C. S., Araya, D. B., McKiernan, G. R., and Wheaton, B. M., "Supersonic Transition Measurements During the BOLT Flight Experiment Descent Phase," AIAA Paper 2022-4099, June-July 2022, <https://doi.org/10.2514/6.2022-4099>.
- <sup>4</sup>Wheaton, B. M., Berridge, D., Wolf, T., Araya, D., Stevens, R., McGrath, B., Kemp, B., and Adamczak, D., "Final Design of the Boundary Layer Transition (BOLT) Flight Experiment," *Journal of Spacecraft and Rockets*, Vol. 58, 2021, pp. 6–17, <https://doi.org/10.2514/1.A34809>.
- <sup>5</sup>Hörschgen-Eggers, M., Kirchhartz, R. M., Jung, W., Schoppmann, K., Ettl, J., and Wittkamp, M., "Boundary Layer Transition Flight Experiment: Mission Overview, Launch Vehicle and Payload Subsystems," *Journal of Spacecraft and Rockets*, Vol. 58, 2021, pp. 26–37, <https://doi.org/10.2514/1.A34877>.
- <sup>6</sup>Berry, S. A., Wheaton, B. M., and Chynoweth, B. C., "Secondary Side Considerations for Boundary Layer Transition Flight Experiment," *Journal of Spacecraft and Rockets*, Vol. 58, 2021, pp. 18–25, <https://doi.org/10.2514/1.A34778>.
- <sup>7</sup>Wirth, J., Morreale, B. J., Bowersox, R. D. W., and Wheaton, B. M., "Boundary Layer Turbulence Flight Experiment in Memory of Mike Holden: Side A Flight Data 2," AIAA Paper 2023-3440, June 2023, <https://doi.org/10.2514/6.2023-3440>.
- <sup>8</sup>Wirth, J., Morreale, B. J., Kostak-Teplicek, H. E., Bowersox, R. D. W., Dufrene, A. T., Portoni, P., and Wadhams, T. P., "Boundary Layer Turbulence Flight Experiment in Memory of Mike Holden: Side A Flight Data," AIAA Paper 2023-0682, January 2023, <https://doi.org/10.2514/6.2023-0682>.
- <sup>9</sup>Berry, S. A. and Wheaton, B. M., "BOLT II Roughness Side Flight Results," AIAA Paper 2023-0684, January 2023, <https://doi.org/10.2514/6.2023-0684>.
- <sup>10</sup>Morreale, B. J., Swinny, E. L., Kostak-Teplicek, H. E., Bowersox, R. D. W., White, E. B., Dufrene, A. T., Wadhams, T. P., Popkin, S., Adamczak, D., and Tancred, J., "Boundary Layer Turbulence Flight Experiment in Memory of Mike Holden: Pre-Flight Mission Design," AIAA Paper 2023-0477, January 2023, <https://doi.org/10.2514/6.2023-0477>.
- <sup>11</sup>McKiernan, G. R., Chynoweth, B. C., Schneider, S. P., Berridge, D. C., and Wheaton, B. M., "Boundary Layer Transition Preflight Experiments in a Mach-6 Quiet Tunnel," *Journal of Spacecraft and Rockets*, Vol. 58, 2021, pp. 54–66, <https://doi.org/10.2514/1.A34772>.
- <sup>12</sup>Yam, C., Schneider, S. P., and Jewell, J. S., "Effects of Forward- and Backward-Facing Steps on Boundary-Layer Transition at Mach 6," AIAA Paper 2022-0346, January 2022, <https://doi.org/10.2514/6.2022-0346>.
- <sup>13</sup>Chynoweth, B. C., Schneider, S. P., and Wheaton, B. M., "Transition Measurements with Forward and Aft Facing Steps on the BOLT Geometry at Mach 6," AIAA Paper 2020-1560, January 2020, <https://doi.org/10.2514/6.2020-1560>.
- <sup>14</sup>Kostak, H. E. and Bowersox, R. D. W., "Preflight Ground Test Analyses of the Boundary Layer Transition (BOLT) Flight Geometry," *Journal of Spacecraft and Rockets*, Vol. 58, 2021, pp. 67–76, <https://doi.org/10.2514/1.A34858>.
- <sup>15</sup>Kostak, H. E., Bowersox, R. D. W., McKiernan, G. R., Thome, J., Candler, G. V., and King, R. A., "Freestream Disturbance Effects on Boundary Layer Instability and Transition on the AFOSR BOLT Geometry," AIAA Paper 2019-0088, January 2019, <https://doi.org/10.2514/6.2019-0088>.
- <sup>16</sup>Berridge, D. C., Kostak, H. E., McKiernan, G. R., King, R. A., Wason, M. P., Wheaton, B. M., Wolf, T. D., and Schneider, S. P., "Hypersonic Ground Tests With High-Frequency Instrumentation In Support of the Boundary Layer Transition (BOLT) Flight Experiment," AIAA Paper 2019-0090, January 2019, <https://doi.org/10.2514/6.2019-0090>.
- <sup>17</sup>Berridge, D. C., McKiernan, G. R., Wadhams, T. P., Holden, M. S., Wheaton, B. M., Wolf, T. D., and Schneider, S. P., "Hypersonic Ground Tests In Support of the Boundary Layer Transition (BOLT) Flight Experiment," AIAA Paper 2018-2893, June 2018, <https://doi.org/10.2514/6.2018-2893>.
- <sup>18</sup>Rieken, E., Berry, S., Mason, M., and Greene, F., "Aerothermodynamic Ground Tests in Support of the Boundary Layer Transition Flight Experiment," *Journal of Spacecraft and Rockets*, Vol. 58, 2021, pp. 38–53, <https://doi.org/10.2514/1.A34803>.
- <sup>19</sup>Dufrene, A. T., Portoni, P., Wadhams, T. P., Kostak-Teplicek, H. E., and Bowersox, R. D. W., "Boundary Layer Turbulence Flight Experiment in Memory of Mike Holden: Vehicle Design, Instrumentation, and Ground Test Results," AIAA Paper 2023-0478, January 2023, <https://doi.org/10.2514/6.2023-0478>.
- <sup>20</sup>Semper, M. T. and Cummings, R. M., "Hypersonic Trip Development for BOLT-II," AIAA Paper 2022-0349, January 2022, <https://doi.org/10.2514/6.2022-0349>.
- <sup>21</sup>Berry, S. A., Semper, M. T., Riha, A. K., Mullen, C. D., Reed, H. L., Dufrene, A. T., and Fasel, H. F., "Development of the BOLT II Roughness Experiment for Flight," AIAA Paper 2022-0347, January 2022, <https://doi.org/10.2514/6.2022-0347>.
- <sup>22</sup>Kostak-Teplicek, H. E. and Bowersox, R. D. W., "Hypersonic Stability and Breakdown Measurements on the AFRL/AFOSR BOLT II Geometry," AIAA Paper 2023-0085, January 2023, <https://doi.org/10.2514/6.2023-0085>.
- <sup>23</sup>Mullen, C. D. and Reed, H. L., "Numerical Simulation of Instabilities in the Boundary-Layer Transition Experiment Flowfield," *Theoretical and Computational Fluid Dynamics*, Vol. 36, 2022, pp. 251–276, <https://doi.org/10.1007/s00162-021-00583-x>.
- <sup>24</sup>Moyes, A. J. and Reed, H. L., "Preflight Boundary-Layer Stability Analysis of BOLT Geometry," *Journal of Spacecraft and Rockets*, Vol. 58, 2021, pp. 78–89, <https://doi.org/10.2514/1.A34792>.

- <sup>25</sup>Moyes, A. and Reed, H. L., “Nonlinear Boundary-Layer Stability Analysis of BOLT and HiFiRE-5,” AIAA Paper 2019-2972, June 2019, <https://doi.org/10.2514/6.2019-2972>.
- <sup>26</sup>Moyes, A., Kocian, T. S., Mullen, C. D., and Reed, H. L., “Pre-Flight Boundary-Layer Stability Analysis of BOLT Geometry,” AIAA Paper 2018-2895, June 2018, <https://doi.org/10.2514/6.2018-2895>.
- <sup>27</sup>Knutson, A., Thome, J., and Candler, G. V., “Numerical Simulation of Instabilities in the Boundary-Layer Transition Experiment Flowfield,” *Journal of Spacecraft and Rockets*, Vol. 58, 2021, pp. 90–99, <https://doi.org/10.2514/1.A34599>.
- <sup>28</sup>Thome, J. S., Knutson, A., and Candler, G. V., “Boundary Layer Instabilities on BoLT Subscale Geometry,” AIAA Paper 2019-0092, January 2019, <https://doi.org/10.2514/6.2019-0092>.
- <sup>29</sup>Cook, D. A., Thome, J. S., Nichols, J. W., and Candler, G. V., “Receptivity analysis of BOLT to distributed surface roughness using input-output analysis,” AIAA Paper 2019-0089, January 2019, <https://doi.org/10.2514/6.2019-0089>.
- <sup>30</sup>Thome, J. S., Dwivedi, A., Nichols, J. W., and Candler, G. V., “Direct numerical simulation of BOLT hypersonic flight vehicle,” AIAA Paper 2018-2894, June 2018, <https://doi.org/10.2514/6.2018-2894>.
- <sup>31</sup>M. M. Choudhari, F. L. and Paredes, P., “A Computational Analysis of Boundary Layer Instability over the BOLT Configuration,” AIAA Paper 2021-1207, January 2021, <https://doi.org/10.2514/6.2021-1207>.
- <sup>32</sup>Li, F., Choudhari, M., and Paredes, P., “Streak Instability Analysis on BOLT Configuration,” AIAA Paper 2020-3028, June 2020, <https://doi.org/10.2514/6.2020-3028>.
- <sup>33</sup>Li, F. and Choudhari, M., “Wake Instability behind Isolated Trip Near the Leading Edge of the BOLT-II Configuration,” AIAA Paper 2022-1063, January 2022, <https://doi.org/10.2514/6.2022-1063>.
- <sup>34</sup>Li, F., Choudhari, M., and Paredes, P., “Transition Analysis for Isolated Trips on BOLT-II Wind-Tunnel and Flight Configurations,” AIAA Paper 2021-2905, August 2021, <https://doi.org/10.2514/6.2021-2905>.
- <sup>35</sup>Johnston, Z. M., Hemati, M. S., and Candler, G. V., “Modal Analysis of Instabilities in the BoLT-2 Flowfield,” AIAA Paper 2022-0348, January 2022, <https://doi.org/10.2514/6.2022-0348>.
- <sup>36</sup>Johnston, Z. M. and Candler, G. V., “Hypersonic simulations of the BoLT-2 subscale geometry,” AIAA Paper 2021-0366, January 2021, <https://doi.org/10.2514/6.2021-0366>.
- <sup>37</sup>Wernz, S., “Flat-BOLT Surrogates for Investigating Second-Mode and Crossflow Instabilities,” AIAA Paper 2023-3442, June 2023, <https://doi.org/10.2514/6.2023-3442>.
- <sup>38</sup>Hill, J. L., Borg, M. P., Tufts, M. W., Benitez, E. K., and Reeder, M. F., “Leading-Edge Curvature Influence on Hypersonic Boundary Layer Transition,” AIAA Paper 2023-0098, January 2023, <https://doi.org/10.2514/6.2023-0098>.
- <sup>39</sup>Davami, J., Juliano, T. J., Chou, A., and Leidy, A. N., “Effect of Roughness on Transition on the BOLT-1a Geometry in Supersonic Flow,” AIAA Paper 2023-3441, June 2023, <https://doi.org/10.2514/6.2023-3441>.
- <sup>40</sup>Beckwith, I. E., Creel, T. R., Chen, F. J., and Kendall, J. M., “Free-Stream Noise and Transition Measurements on a Cone in a Mach 3.5 Pilot Low-Disturbance Tunnel,” NASA TP 2180, September 1983, <https://doi.org/10.2514/6.2060/19830025958>.
- <sup>41</sup>Laufer, J., “Aerodynamic Noise in Supersonic Wind Tunnels,” *Journal of the Aerospace Sciences*, Vol. 28, 1961, pp. 685–692, <https://doi.org/10.2514/8.9150>.
- <sup>42</sup>Schneider, S. P., “Development of Hypersonic Quiet Tunnels,” *Journal of Spacecraft and Rockets*, Vol. 45, 2008, pp. 641–664, <https://doi.org/10.2514/1.34489>.
- <sup>43</sup>Berger, K., Rufer, S., Hollingsworth, K., and Wright, S., “NASA Langley Aerothermodynamics Laboratory: Hypersonic Testing Capabilities,” AIAA Paper 2015-1337, January 2015, <https://doi.org/10.2514/6.2015-1337>.
- <sup>44</sup>Boyd, C. and Howell, A., “Numerical Investigation of One-Dimensional Heat-Flux Calculations,” Technical report, Naval Surface Warfare Center Dahlgren Division, Silver Spring, MD, 1994.
- <sup>45</sup>Owens, L. R., Kegerise, M. A., and Wilkinson, S. P., “Off-Body Boundary-Layer Measurement Techniques Development for Supersonic Low-Disturbance Flows,” AIAA Paper 2011-0284, January 2011, <https://doi.org/10.2514/6.2011-0284>.
- <sup>46</sup>Kegerise, M. A., Owens, L. R., and King, R. A., “High-Speed Boundary-Layer Transition Induced by an Isolated Roughness Element,” AIAA Paper 2010-4999, June-July 2010, <https://doi.org/10.2514/6.2010-4999>.
- <sup>47</sup>Freythuth, P., “Noise in Hot-Wire Anemometers,” *The Review of Scientific Instruments*, Vol. 39, 1968, pp. 550–557, <https://doi.org/10.1063/1.1683430>.
- <sup>48</sup>Kostak, H., *Ground Test Analyses of the AFOSR Boundary Layer Transition (BOLT) Flight Geometry*, Master’s thesis, Texas A&M University, 2020.